

# NOBEYAMA MILLIMETER INTERFEROMETRIC HCN(1–0) AND HCO<sup>+</sup>(1–0) OBSERVATIONS OF FURTHER LUMINOUS INFRARED GALAXIES

MASATOSHI IMANISHI<sup>1</sup>

National Astronomical Observatory, 2-21-1, Osawa, Mitaka, Tokyo 181-8588, Japan

KOUCIHIRO NAKANISHI<sup>1</sup>

Nobeyama Radio Observatory, Minamimaki, Minamisaku, Nagano, 384-1305, Japan

YOICHI TAMURA<sup>2</sup>

Department of Astronomy, The University of Tokyo, 7-3-1 Hongo, Bunkyo-ku, Tokyo 113-0033, Japan

AND

CHIH-HAN PENG

formerly Department of Astronomy, School of Science, Graduate University for Advanced Studies, Mitaka, Tokyo 181-8588  
*Astronomical Journal*

## ABSTRACT

We report the results of interferometric HCN(1–0) and HCO<sup>+</sup>(1–0) observations of four luminous infrared galaxies (LIRGs), NGC 2623, Mrk 266, Arp 193, and NGC 1377, as a final sample of our systematic survey using the Nobeyama Millimeter Array. Our survey contains the most systematic *interferometric, spatially-resolved, simultaneous* HCN(1–0) and HCO<sup>+</sup>(1–0) observations of LIRGs. Ground-based infrared spectra of these LIRGs are also presented to elucidate the nature of the energy sources at the nuclei. We derive the HCN(1–0)/HCO<sup>+</sup>(1–0) brightness-temperature ratios of these LIRGs and confirm the previously discovered trend that LIRG nuclei with luminous buried AGN signatures in infrared spectra tend to show high HCN(1–0)/HCO<sup>+</sup>(1–0) brightness-temperature ratios, as seen in AGNs, while starburst-classified LIRG nuclei in infrared spectra display small ratios, as observed in starburst-dominated galaxies. Our new results further support the argument that the HCN(1–0)/HCO<sup>+</sup>(1–0) brightness-temperature ratio can be used to observationally separate AGN-important and starburst-dominant galaxy nuclei.

*Subject headings:* galaxies: active — galaxies: nuclei — galaxies: ISM — radio lines: galaxies — galaxies: individual (NGC 2623, Mrk 266, Arp 193, and NGC 1377)

## 1. INTRODUCTION

Luminous infrared galaxies (LIRGs) radiate the bulk of their large luminosities ( $L > 10^{11} L_{\odot}$ ) as infrared dust emission. Large infrared luminosities mean that: (1) luminous energy sources are present, but are hidden behind dust; (2) energetic radiation from the hidden energy sources is absorbed by the surrounding dust; and (3) the heated dust grains re-emit this energy as infrared thermal radiation. To understand the nature of LIRGs, it is essential to unveil the hidden energy sources; namely, to distinguish whether starbursts (= nuclear fusion inside stars) are dominant, or active galactic nuclei (AGNs; active mass accretion onto a central compact supermassive black hole [SMBH] with  $>10^6 M_{\odot}$ ) are also energetically important.

Unlike AGNs surrounded by toroidally shaped dust, which are classified optically as Seyferts (Veilleux & Osterbrock 1987), concentrated molecular gas and dust in LIRG nuclei (Sanders & Mirabel 1996) can easily *bury* (= obscure in virtually all directions) the putative compact AGNs, making AGN signatures very difficult to detect

optically. However, it is crucial to understand the energetic role of such optically elusive *buried* AGNs in LIRG nuclei.

A starburst (nuclear fusion) and buried AGN (mass accretion onto a SMBH) have very different energy generation mechanisms. Specifically, while UV emission is predominant in a starburst, an AGN emits strong X-ray emission in addition to UV. Additionally, in a normal starburst, the stellar energy sources and dust are spatially well mixed, so energy sources are spatially extended. Since the energy generation efficiency of the nuclear fusion reaction is only  $\sim 0.5\%$  of  $Mc^2$  ( $M$  is the mass of material used in the nuclear fusion reaction), the emission surface brightness of a starburst is modest and has both observational (Soifer et al. 2000) and theoretical (Thompson et al. 2005) upper limits ( $\sim 10^{13} L_{\odot} \text{ kpc}^{-2}$ ). On the other hand, in an AGN, the mass accreting SMBH is spatially very compact, and thus more centrally concentrated than the surrounding gas and dust. The high energy generation efficiency of an AGN (6–42% of  $Mc^2$ ;  $M$  is the mass of accreting material; Thorne 1974) can generate large luminosities from a very compact region, producing a very high emission surface brightness (Soifer et al. 2000). These differences between an AGN and a starburst could create differences in the properties of the surrounding molecular gas and dust that may be distin-

Electronic address: masa.imanishi@nao.ac.jp

<sup>1</sup> Department of Astronomy, School of Science, Graduate University for Advanced Studies, Mitaka, Tokyo 181-8588

<sup>2</sup> National Astronomical Observatory of Japan, 2-21-1 Osawa, Mitaka, Tokyo 181-8588, Japan

guishable based on observations at wavelengths of low dust extinction.

Molecular gas emission lines in the millimeter wavelength range can be used effectively to investigate the hidden energy sources of LIRG nuclei. First, dust extinction is very small. Second, theoretical calculations predict that X-ray- and UV-emitting energy sources show different behaviors of molecular line emission due to different chemical reactions (Meijerink et al. 2006). Finally, mid-infrared 10–20  $\mu\text{m}$  emission is strong in an AGN because of hot dust thermal emission heated by the high surface brightness energy source of an AGN. The strong mid-infrared emission could selectively enhance particular molecular line emission through an infrared radiative pumping mechanism (Aalto et al. 1995; Garcia-Burillo et al. 2006; Guelin et al. 2007; Weiss et al. 2007; Aalto et al. 2007). In this paper, we focus on HCN(1–0) and HCO<sup>+</sup>(1–0) lines, because an AGN could enhance HCN(1–0) emission through an increased HCN abundance (Lintott & Viti 2006) and/or infrared radiative pumping (Aalto et al. 1995; Garcia-Burillo et al. 2006; Weiss et al. 2007). In fact, Kohno (2005) found observationally that HCN(1–0) emission is stronger, relative to HCO<sup>+</sup>(1–0), in AGN-dominated nuclei than in starburst galaxies, demonstrating the potential of this HCN(1–0) and HCO<sup>+</sup>(1–0) based method for the purpose of distinguishing between an AGN and a starburst. This method may be effective even for a Compton thick ( $N_{\text{H}} > 10^{24} \text{ cm}^{-2}$ ) buried AGN, the detection of which is very difficult with direct X-ray observations.

HCN(1–0) and HCO<sup>+</sup>(1–0) observations of a large number of LIRGs have been made, using single-dish radio telescopes (Gao & Solomon 2004; Gracia-Carpio et al. 2008; Krips et al. 2008). However, the beam sizes of these observations are so large (>25 arcsec) that severe contamination from spatially-extended star-forming emission is unavoidable, possibly hampering the detection of the AGN signatures of LIRG nuclei, where putative AGNs are expected to be present. Furthermore, LIRGs often show multiple-nucleus morphologies with small separations (<10 arcsec), for which spatially-resolved study is not possible with single-dish radio telescopes. Finally, the HCN(1–0) and HCO<sup>+</sup>(1–0) data were collected at different times under different weather conditions, possibly increasing uncertainty regarding their relative strengths due to the ambiguity of inter-calibration of data.

To overcome these issues, we performed millimeter *interferometric, spatially-resolved, simultaneous* HCN(1–0) and HCO<sup>+</sup>(1–0) observations of LIRGs, using the Nobeyama Millimeter Array (NMA) (Imanishi et al. 2004, 2006b; Imanishi & Nakanishi 2006; Imanishi et al. 2007b). In our study, only nuclear HCN(1–0) and HCO<sup>+</sup>(1–0) emission was extracted to investigate their ratios in brightness temperature ( $\propto \text{flux} \times \lambda^2$ ). The sample contained mostly ultraluminous infrared galaxies (ULIRGs;  $L_{\text{IR}} > 10^{12} L_{\odot}$ ; Sanders et al. 1988a) showing luminous buried AGN signatures at other wavelengths, and we found that their HCN(1–0)/HCO<sup>+</sup>(1–0) brightness-temperature ratios were generally higher than starburst galaxies with  $L_{\text{IR}} < 10^{12} L_{\odot}$ . This result supports the presence of luminous buried AGNs in these observed ULIRGs. However, scenarios that try to explain large HCN(1–0)/HCO<sup>+</sup>(1–0) brightness-

temperatures ratios, without invoking luminous AGNs, have been present. Examples include the high turbulence (Papadopoulos 2007) or high density (Imanishi et al. 2007b) of molecular gas. In fact, ULIRGs have very dense, highly disturbed molecular gas compared to normal LIRGs with  $L_{\text{IR}} < 10^{12} L_{\odot}$  (i.e., non-ULIRGs) (Sanders & Mirabel 1996; Soifer et al. 2000, 2001). Observations of normal LIRGs (non-ULIRGs), with or without buried AGN signatures, would help elucidate whether the high HCN(1–0)/HCO<sup>+</sup>(1–0) brightness-temperature ratios in observed ULIRGs are indeed caused by luminous buried AGNs, or are simply due to different molecular gas properties in ULIRGs.

In this paper, we present the results of interferometric, simultaneous HCN(1–0) and HCO<sup>+</sup>(1–0) observations of such normal LIRGs (non-ULIRGs), to investigate the HCN(1–0)/HCO<sup>+</sup>(1–0) brightness-temperature ratios in the nuclear regions. This is the final paper of our series of interferometric HCN(1–0) and HCO<sup>+</sup>(1–0) surveys of LIRGs using NMA (Imanishi et al. 2004, 2006b; Imanishi & Nakanishi 2006; Imanishi et al. 2007b). Ancillary ground-based infrared *K*- (1.9–2.5  $\mu\text{m}$ ) and *L*- (2.8–4.1  $\mu\text{m}$ ) band spectra are also utilized to better understand the hidden energy sources of these millimeter-observed LIRG nuclei. Throughout this paper, we adopt  $H_0 = 75 \text{ km s}^{-1} \text{ Mpc}^{-1}$ ,  $\Omega_{\text{M}} = 0.3$ , and  $\Omega_{\Lambda} = 0.7$ , to be consistent with our previously published papers.

## 2. TARGETS

We observed the four LIRGs, NGC 2623, Mrk 266, Arp 193, and NGC 1377, primarily because they were non-ULIRGs with or without buried AGN signatures and so were appropriate sources to address the above-mentioned issue (§1), and because we estimated that we could detect HCN(1–0) and HCO<sup>+</sup>(1–0) emission with NMA in a reasonable amount of telescope time. Table 1 summarizes the infrared emission properties of these LIRGs. An angular scale of 1'' corresponds to a physical size of 0.12–0.53 kpc at the redshifts of these LIRGs ( $z = 0.006$ –0.028).

NGC 2623 ( $z = 0.018$ ) is a LIRG ( $L_{\text{IR}} = 10^{11.5} L_{\odot}$ ) with two prominent merging tails along the north-eastern and south-western directions (Rothberg & Joseph 2004). It is optically unclassified (Keel 1984; Veilleux et al. 1995); no obvious AGN signature exists in the optical spectrum. Its infrared 5–35  $\mu\text{m}$  spectrum obtained with *Spitzer* IRS is dominated by polycyclic aromatic hydrocarbon (PAH) emission, as is usually observed in starburst galaxies (Brandl et al. 2006). However, high spatial resolution ground-based infrared 10- $\mu\text{m}$  imaging observations reveal that the bulk of the 10- $\mu\text{m}$  emission in NGC 2623 comes from compact nuclear cores with <400 pc, the surface brightness of which can be as high as  $\sim 10^{13} L_{\odot}$  (Soifer et al. 2001). This value is close to the maximum found in starburst phenomena (Soifer et al. 2000). The 2–10 keV X-ray emission from NGC 2623 is characterized by a hard spectrum, suggesting that the scattered component of X-ray emission from a Compton thick ( $N_{\text{H}} > 10^{24} \text{ cm}^{-2}$ ) AGN dominates the observed 2–10 keV X-ray flux (Maiolino et al. 2003). The intrinsic AGN luminosity is highly dependent on the unknown value of the scattering efficiency, and can be high if the efficiency is low. The optical non-detection of Seyfert signatures in NGC 2623 suggests that the putative AGN is a buried

one, whose scattering efficiency is expected to be low (Fabian et al. 2002). Evans et al. (2008) performed multi-wavelength observations of NGC 2623, and detected the high-excitation forbidden-emission line [NeV]14.3 $\mu$ m in the infrared, indicative of narrow line region clouds photoionized by AGN radiation. The intrinsic AGN luminosity can be high because the narrow line regions are expected to be under-developed in a buried AGN (Imanishi et al. 2006a, 2007a). The high CO(1–0) flux at the core of NGC 2623 (Bryant & Scoville 1999) suggests that detection of nuclear HCN(1–0) emission is feasible.

Mrk 266 (NGC 5256;  $z = 0.028$ ) is a LIRG ( $L_{\text{IR}} = 10^{11.5}L_{\odot}$ ), consisting of two main merging nuclei separated by  $\sim 10$  arcsec, a south-western (SW) and north-eastern (NE) nucleus (Mazzarella & Boroson 1993). Optical spectroscopy by various groups suggested that the SW nucleus shows clear Seyfert 2 signatures but the NE one does not (Osterbrock & Dahari 1983; Kollatschny & Fricke 1984; Mazzarella & Boroson 1993; Wu et al. 1998; Goncalves et al. 1999; Ishigaki et al. 2000). However, the most systematic optical spectral classification of galaxies classified the SW and NE nuclei of Mrk 266 as LINER and Seyfert 2, respectively (Veilleux et al. 1995). High spatial resolution X-ray data obtained with *Chandra* found that the X-ray spectrum of the NE nucleus is characterized by a heavily-obscured AGN, while that of the SW nucleus consists of an obscured AGN and a strong starburst component (Brassington et al. 2007). The detection of a strong 3.3- $\mu$ m PAH emission feature (Imanishi 2002), a good starburst indicator (Moorwood 1986; Imanishi & Dudley 2000), supports the presence of a strong starburst in the SW nucleus. The radio 8.44-GHz (3.55 cm) to infrared (1–1000  $\mu$ m) luminosity ratio of Mrk 266 is a factor of 2–3 higher than other LIRGs, suggesting the presence of a radio-intermediate (or radio-loud) AGN (Condon et al. 1991). The radio emission of the NE nucleus is dominated by a spatially compact ( $< 0''.3$ ) component and is much brighter than that of the SW nucleus (Condon et al. 1991). The infrared 5–35  $\mu$ m spectrum, taken with *Spitzer* IRS, is dominated by large equivalent-width PAH emission, which is typical of starburst galaxies (Brandl et al. 2006). However, we note that the SW and NE nuclei are not sufficiently covered with SL (5.2–14.5  $\mu$ m) and LL (14–38  $\mu$ m) spectra, respectively (Brandl et al. 2006), possibly missing AGN signatures, given the lack of full *Spitzer* spectral coverage for both nuclei.

Arp 193 ( $z=0.023$ ) is a LIRG ( $L_{\text{IR}} = 10^{11.6}L_{\odot}$ ) with a long narrow tail along the south-eastern direction (Rothberg & Joseph 2004). It is classified optically as a LINER (Veilleux et al. 1995), showing no obvious optical AGN signatures. The mid-infrared 8–20  $\mu$ m dust emission is dominated by a spatially-extended component with no prominent compact core (Soifer et al. 2001). The emission surface brightness is  $\sim 2 \times 10^{12}L_{\odot}$  (Soifer et al. 2001), which is within the range of starburst phenomena. The HCN(1–0) and HCO<sup>+</sup>(1–0) fluxes of Arp 193, measured with single-dish radio telescopes, are high (Solomon et al. 1992; Gracia-Carpio et al. 2008). Millimeter interferometric observations revealed that the CO(1–0) emission shows a strong nuclear compact component (Downes & Solomon 1998; Bryant & Scoville 1999). Hence, we expect that detection of nuclear HCN(1–0) emission is feasible if the nuclear to

extended flux ratio for the HCN(1–0) line is similar to or higher than that of the CO(1–0) line. Papadopoulos (2007) found that the HCN(4–3) to HCN(1–0) flux ratio of Arp 193 is much lower than that of other LIRGs. The weak high-excitation HCN(4–3) line may suggest that the dominant energy source is a spatially-extended diffuse one, rather than a compact high-emission surface-brightness one. So far, no obvious AGN signatures have been seen in the Arp 193 observational data (Vega et al. 2008).

NGC 1377 ( $z=0.006$ ) has an infrared luminosity of  $L_{\text{IR}} = 10^{10.1}L_{\odot}$ , and so is not a LIRG in a strict sense. This galaxy shows a deficit of 21-cm emission relative to infrared emission (Roussel et al. 2003). Although it is optically unclassified (Veilleux et al. 1995), and thus no AGN signatures are present in the optical spectrum, the infrared 3–25  $\mu$ m spectrum is dominated by a PAH-free continuum (Imanishi 2006; Roussel et al. 2006), typical of AGN-dominated galaxies. The 9.7- $\mu$ m and 18- $\mu$ m silicate dust absorption features are extremely strong (Roussel et al. 2006), suggesting that the putative AGN is deeply buried in dust. NGC 1377 is included in our sample to investigate whether even a buried AGN candidate with low absolute infrared luminosity can have a high HCN(1–0)/HCO<sup>+</sup>(1–0) brightness-temperature ratio. This inclusion is important to test whether the general trend of high HCN(1–0)/HCO<sup>+</sup>(1–0) brightness-temperature ratios found in ULIRGs with buried AGN signatures (Imanishi et al. 2006b, 2007b) is indeed due to AGN-related phenomena, or simply the result of extreme molecular gas properties in ULIRGs (see §1). The CO(1–0) emission is detected with single-dish radio telescope observations (Roussel et al. 2003). If a significant fraction of the CO(1–0) emission comes from the nuclear regions, and unless the nuclear HCN(1–0)/CO(1–0) brightness-temperature ratio is extremely low, then we estimate that detection of nuclear HCN(1–0) emission is feasible.

### 3. OBSERVATIONS AND DATA REDUCTION

#### 3.1. Millimeter Interferometry

We performed interferometric observations of LIRGs, at HCN(1–0) ( $\lambda_{\text{rest}} = 3.3848$  mm and  $\nu_{\text{rest}} = 88.632$  GHz) and HCO<sup>+</sup>(1–0) ( $\lambda_{\text{rest}} = 3.3637$  mm or  $\nu_{\text{rest}} = 89.188$  GHz) lines, using the Nobeyama Millimeter Array (NMA) at the Nobeyama Radio Observatory (NRO) between 2006 December and 2008 March. For Mrk 266 and NGC 1377, since no interferometric CO(1–0) maps had been published, we conducted NMA observations at CO(1–0) ( $\lambda_{\text{rest}} = 2.6026$  mm or  $\nu_{\text{rest}} = 115.271$  GHz). Table 2 summarizes the detailed observing log. The NMA consists of six 10-m antennas and observations were undertaken using the AB (the longest baseline was 351 m), C (163 m), and D (82 m) configurations.

The backend was the Ultra-Wide-Band Correlator (UWBC) (Okumura et al. 2000) which can cover 1024 MHz with 128 channels at 8-MHz resolution. For HCN(1–0) and HCO<sup>+</sup>(1–0) observations, the central frequency for each source (Table 2) was set to cover both the redshifted HCN(1–0) and HCO<sup>+</sup>(1–0) lines simultaneously. A bandwidth of 1024 MHz corresponds to  $\sim 3500$  km s<sup>−1</sup> for the redshifted HCN(1–0) and HCO<sup>+</sup>(1–0) lines at  $\nu \sim 86$ –89 GHz and  $\sim 2700$  km s<sup>−1</sup> for the redshifted CO(1–0) lines at  $\nu \sim 112$ –115 GHz. The fields

of view at 86–89 GHz and 112–115 GHz are  $\sim 77''$  and  $\sim 62''$  at full-width at half-maximum (FWHM), respectively. The Hanning window function was applied to reduce side lobes in the spectra, so that the effective resolution was widened to 16 MHz or  $54 \text{ km s}^{-1}$  ( $42 \text{ km s}^{-1}$ ) at  $\nu \sim 86\text{--}89 \text{ GHz}$  ( $112\text{--}115 \text{ GHz}$ ).

The UVPROC-II package developed at NRO (Tsumi et al. 1997) and the AIPS package of the National Radio Astronomy Observatory were used for standard data reduction. Corrections for the antenna baselines, band-pass properties, and time variation in the visibility amplitude and phase were applied to all of the data (Table 2). After discarding a fraction of the data with large phase scatter due to poor millimeter seeing and clipping a small fraction of data with unusually high amplitude, the data were Fourier-transformed using a natural  $UV$  weighting. The flux calibration was made using observations of Uranus or appropriate quasars whose flux levels had been measured at least every month in the NMA observing seasons (Table 2). A conventional CLEAN method was applied to deconvolve the synthesized beam pattern. Table 3 summarizes the total net on-source integration times and synthesized beam patterns.

### 3.2. Ground-based Infrared $K$ - ( $1.9\text{--}2.5 \mu\text{m}$ ) and $L$ - ( $2.8\text{--}4.1 \mu\text{m}$ ) band Spectroscopy

To put stronger constraints on the hidden energy sources at these millimeter-observed LIRG nuclei, we performed ground-based infrared  $K$ - ( $1.9\text{--}2.5 \mu\text{m}$ ) and  $L$ - ( $2.8\text{--}4.1 \mu\text{m}$ ) band spectroscopy of NGC 2623, Mrk 266, and Arp 193, as their  $L$ -band spectra were not available in the literature. NGC 1377 was not observed, because its  $L$ -band spectrum was given by Imanishi (2006).

In short, through infrared  $L$ -band spectroscopy, we can investigate the energy sources based on the equivalent width of the  $3.3 \mu\text{m}$  PAH emission and the optical depths of absorption features at  $\lambda_{\text{rest}} \sim 3.05 \mu\text{m}$  by ice-covered dust grains and at  $\lambda_{\text{rest}} \sim 3.4 \mu\text{m}$  by bare carbonaceous dust grains (Imanishi & Dudley 2000; Imanishi & Maloney 2003; Imanishi et al. 2006a). A normal starburst galaxy should always show large equivalent-width  $3.3 \mu\text{m}$  PAH emission, while a pure AGN produces a PAH-free continuum (Imanishi & Dudley 2000; Imanishi et al. 2006a). For absorption features, optical depths have upper limits in a normal starburst in which stellar energy sources and dust are spatially well mixed, while the depths can be arbitrarily large in a buried AGN with a more centrally concentrated energy source geometry than the surrounding dust (Imanishi & Maloney 2003; Imanishi et al. 2006a). In the infrared  $K$ -band spectra, emission from stars and AGNs is distinguishable using CO absorption features at  $\lambda_{\text{rest}} = 2.3\text{--}2.4 \mu\text{m}$  because the CO absorption features are produced by stars older than  $10^6 \text{ yr}$ , but not by AGN-heated hot dust emission.

Infrared  $K$ - ( $1.9\text{--}2.5 \mu\text{m}$ ) and  $L$ - ( $2.8\text{--}4.1 \mu\text{m}$ ) band spectra were taken using SpeX (Rayner et al. 2003) attached to the IRTF 3-m telescope atop Mauna Kea, Hawaii, on 2008 Apr 19 and 20 (UT). The  $1.9\text{--}4.2 \mu\text{m}$  cross-dispersed mode was employed, so that  $K$ - and  $L$ -band spectra were obtained simultaneously. We chose a narrow  $0''.8$ -wide slit to pinpoint the infrared continuum emission peaks of individual LIRG nuclei where the putative AGN may be located. The resulting spectral resolution using this slit is  $R \sim 1000$  in the  $K$ - and  $L$ -

bands.

Photometric conditions persisted throughout the observations. The seeing at  $K$  was measured in the range  $0''.6\text{--}0''.8$  in FWHM. A standard telescope nodding technique (ABBA pattern) with a throw of  $7''.5$  was employed along the slit. Each exposure was 15 sec, and two coadds were made at each position. The telescope tracking was monitored with the SpeX infrared slit-viewer. Table 4 summarizes the detailed observing log.

Appropriate standard stars (Table 4), with an airmass difference of  $<0.1$  for individual LIRGs, were observed to correct for the wavelength-dependent transmission of Earth's atmosphere. The  $K$ - and  $L$ -band magnitudes of the standard stars were estimated based on their  $V$ -band ( $0.6 \mu\text{m}$ ) magnitudes, and  $V - K$  and  $V - L$  colors, of the corresponding stellar types (Tokunaga 2000). The estimated  $K$ -band magnitudes agree very well with the 2MASS measurements (Skrutskie et al. 2006).

Standard data reduction procedures were employed using IRAF<sup>3</sup>. Initially, frames taken with an A (or B) beam were subtracted from frames subsequently taken with a B (or A) beam, and the resulting subtracted frames were added and divided by a spectroscopic flat image. Then, bad pixels and pixels hit by cosmic rays were replaced with interpolated values from surrounding pixels. Finally the spectra of LIRG nuclei and standard stars were extracted by integrating signals over  $1''.8\text{--}2''.7$ , depending on actual signal profiles. Wavelength calibration was performed based on standard star spectra which reflect the wavelength-dependent nature of Earth's atmospheric transmission curve with high signal-to-noise ratios. The LIRG nuclei spectra were divided by the observed spectra of standard stars, and then multiplied by the spectra of blackbodies with temperatures appropriate to individual standard stars (Table 4).

Flux calibration was done based on signals of LIRGs and standard stars detected inside our slit spectra. Since we employed a narrow  $0''.8$ -wide slit, our spectra are sensitive only to spatially-compact emission, and miss a spatially-extended component. To reduce data point scatter, appropriate binning of spectral elements was performed.

## 4. RESULTS

### 4.1. Millimeter Interferometric Data

For NGC 2623, Mrk 266, and Arp 193, our spectra at the HCN(1–0) or HCO<sup>+</sup>(1–0) emission peaks show that the flux levels between these lines are above zero, indicating that continuum emission is present. We combined data points that are unaffected by these lines and made interferometric maps of the continuum emission. Figure 1 presents the contours of the continuum emission for NGC 2623, Mrk 266, and Arp 193, in the vicinity of the redshifted HCN(1–0) and HCO<sup>+</sup>(1–0) emission at 86–89 GHz. For Arp 193, the continuum emission ( $\sim 15 \text{ mJy}$ ) is clearly ( $>8\sigma$ ) detected. For NGC 2623, and Mrk 266 SW and NE, signs of continuum emission are marginally seen ( $\sim 3\sigma$ ). Continuum emission was not detected in the HCN(1–0)/HCO<sup>+</sup>(1–0) data of NGC 1377, or the

<sup>3</sup> IRAF is distributed by the National Optical Astronomy Observatories, operated by the Association of Universities for Research in Astronomy, Inc. (AURA), under cooperative agreement with the National Science Foundation.

CO(1–0) data of Mrk 266 and NGC 1377.

Figure 2 displays integrated intensity maps of the HCN(1–0) and HCO<sup>+</sup>(1–0) emission of the observed four LIRGs. Figure 3 presents the interferometric maps of CO(1–0) emission for Mrk 266 and NGC 1377. Since LIRGs contain highly concentrated nuclear molecular gas (Sanders & Mirabel 1996), the fraction of high-density molecular gas ( $n_{\text{H}} > 10^4 \text{ cm}^{-3}$ ) is expected to increase (Gao & Solomon 2004). Such molecular gas is better probed with HCN(1–0) and HCO<sup>+</sup>(1–0) rather than the widely used CO(1–0) because the dipole moments of HCN and HCO<sup>+</sup> ( $\mu > 3$  debye) are much larger than CO ( $\mu \sim 0.1$  debye; Botschwina et al. 1993; Millar et al. 1997). Hence, the maps in Fig. 2 reflect the spatial distribution of the dense molecular gas phase.

Mrk 266 has a double-nucleus morphology. The CO(1–0) emission is sufficiently bright to investigate its velocity information for each individual nucleus, as shown in Figure 4. In this CO(1–0) channel map (Fig. 4), the NE nucleus shows a CO(1–0) emission peak at lower frequency (112.08–112.11 GHz) than the SW nucleus (112.17–112.19 GHz), suggesting that the NE nucleus is more redshifted than the SW nucleus. Previously obtained optical spectra also show that the NE nucleus is more redshifted than the SW nucleus (20–130 km s<sup>−1</sup>) (Mazzarella & Boroson 1993; Kollatschny & Fricke 1984; Kim et al. 1995).

Figure 5 shows spectra around the HCN(1–0) and HCO<sup>+</sup>(1–0) lines at the nuclear positions of the observed four LIRGs. Spectra around the CO(1–0) line for Mrk 266 SW and NE, and NGC 1377 are presented in Figure 6. For NGC 1377, HCN(1–0) emission might be marginally detected in the integrated intensity map close to the CO(1–0) emission peak (Figs. 2 and 3). In the spectrum at this peak position, five successive spectral elements at the expected HCN(1–0) frequency show flux excess, compared to the surrounding pixels (Fig. 5, lower-left). For reference, a spectrum with less binning, despite being slightly noisier, also displays signatures of HCN(1–0) emission (Fig. 5, lower-right). We thus regard the HCN(1–0) emission signature as real in NGC 1377.

Figure 7 presents Gaussian fits to the detected HCN(1–0), HCO<sup>+</sup>(1–0), and CO(1–0) lines. In the HCN(1–0)/HCO<sup>+</sup>(1–0) spectra, the central velocity and line width of the Gaussian components are determined independently for both lines. For NGC 1377, although HCN(1–0) and CO(1–0) emission are seen in similar positions (Figs. 2 and 3), their velocity profiles are significantly different (Fig. 7). It may be that the HCN(1–0) line reflects high density molecular gas in the central nuclear region of NGC 1377, while CO(1–0) emission probes the surrounding diffuse molecular gas toward the nuclear direction. We should take care interpreting the HCN(1–0)/CO(1–0) brightness-temperature ratio of NGC 1377 because HCN(1–0) and CO(1–0) lines may probe physically unrelated molecular gas components.

Table 5 summarizes the derived Gaussian fitting parameters. The derived fluxes of HCN(1–0) and HCO<sup>+</sup>(1–0), and their brightness-temperature ratios at the nuclear peak positions (i.e., spatially unresolved component) are also summarized in Table 5. For NGC 2623 and Arp 193, where continuum emission is subtracted, the integrated HCN(1–0) and HCO<sup>+</sup>(1–0) fluxes are also estimated from the peak contours of the integrated intensity

maps in Fig. 2. The values estimated in this way agree with those based on the Gaussian fits to within 30%. Table 5 also includes CO(1–0) fluxes at the nuclear peaks, derived from our NMA data (Mrk 266 and NGC 1377) or taken from the literature (NGC 2623 and Arp 193).

The CO(1–0) emission at Mrk 266 SW clearly displays spatially-extended structures (Fig. 3). The total CO(1–0) flux, including this spatially-extended component, is estimated to be 162 Jy km s<sup>−1</sup>.

CO(1–0) fluxes of Mrk 266 and NGC 1377, and HCN(1–0) and HCO<sup>+</sup>(1–0) fluxes of Arp 193, have been measured using single-dish radio telescopes (Sanders et al. 1986; Roussel et al. 2003; Gracia-Carpio et al. 2008). Table 6 compares these single-dish measurements with our NMA interferometric data. For Mrk 266 CO(1–0) emission, our interferometric flux measurements provide good agreement, within  $\sim 15\%$ , to old single-dish measurements. For Arp 193, our HCN(1–0) flux is more comparable to the latest IRAM 30m measurement (Gracia-Carpio et al. 2008), but is a factor of two smaller than the old IRAM one (Solomon et al. 1992), whose high flux measurement was noted by Gracia-Carpio et al. (2008). For Arp193 HCO<sup>+</sup>(1–0) emission, our measurement agrees with the latest IRAM 30m data (Gracia-Carpio et al. 2008). For these lines, the bulk of the emission should be covered in our interferometric data. For the nearest source, NGC 1377, however, our CO(1–0) flux measurement is more than a factor of four smaller than the SEST telescope measurement, suggesting that our interferometric data miss a spatially very extended component, and detect only nuclear compact molecular gas.

#### 4.2. Ground-based Infrared Spectra

Figure 8 presents ground-based infrared *K*- (1.9–2.5  $\mu\text{m}$ ) and *L*- (2.8–4.1  $\mu\text{m}$ ) band spectra of NGC 2623, Mrk 266 SW and NW, and Arp 193. *K*-band spectra with narrower wavelength coverage are available for NGC 2623, Arp 193, and Mrk 266 SW (Ridgway et al. 1994; Goldader et al. 1997). For Mrk 266 SW, an *L*-band spectrum is also available (Imanishi 2002). A *K*-band spectrum of Mrk 266 NE, and *L*-band spectra of NGC 2623, Mrk 266 NE, and Arp 193 are first presented in this paper. For Mrk 266, this is the first infrared spectrum that clearly resolves emission from the Mrk 266 NE and SW nuclei, allowing separate investigation of the energy sources of individual nuclei for the first time.

##### 4.2.1. Continuum Flux Level

For NGC 2623, and Mrk 266 NE and SW, the *K*-band flux levels of our SpeX spectra (0.8 slit width) are a factor of 1.7–2.7 smaller than the *K*-band photometric measurements with a 5" aperture (Carico et al. 1990). For NGC 2623, Mrk 266 SW, and Arp 193, the *K*-band flux levels of our SpeX spectra (0.8 slit width) are 30–50% smaller than those measured in 3"  $\times$  9" aperture spectra (Goldader et al. 1997). The difference is greatest for Mrk 266 SW, whose spatially-extended *K*-band emission is strongest in our spectra along the slit direction. The smaller flux levels in our spectra are reasonable, given that our smaller aperture misses a spatially extended emission component.

##### 4.2.2. Hydrogen Recombination Lines

Strong Pa $\alpha$  (1.87  $\mu\text{m}$ ) and Br $\alpha$  (4.05  $\mu\text{m}$ ) emission lines are visible in some spectra. Enlarged spectra around these strong emission lines are shown in Figure 9. In the  $K$ -band spectra, Br $\gamma$  (2.17  $\mu\text{m}$ ) and H $_2$ (1–0) S(1) (2.12  $\mu\text{m}$ ) emission lines are detectable. Table 7 summarizes the strengths and line widths of these emission lines. If emission from the broad line regions close to the central SMBH in an AGN is strong and only modestly obscured, then we may be able to detect broad (FWHM  $> 1500 \text{ km s}^{-1}$ ) emission line components in the infrared, where dust extinction is much smaller than the optical, as was seen in optical Seyfert 2 galaxies (Hill et al. 1996; Veilleux et al. 1997; Lutz et al. 2002). However, we see no obvious signatures of broad line components. Since buried AGNs tend to contain a larger amount of obscuring dust than Seyfert 2 AGNs (Imanishi et al. 2006a, 2007a, 2008), detection of the broad emission line components would be more difficult, even if the buried AGNs emit intrinsically luminous broad emission lines.

In Table 7, since our small aperture spectra miss spatially-extended emission, the absolute flux is not meaningful. Only the flux ratios between different emission lines measured with the same apertures will be used in our discussion.

#### 4.2.3. PAH Emission

The 3.3- $\mu\text{m}$  PAH emission is clearly seen in the  $L$ -band spectra of all the observed LIRGs. To estimate the 3.3- $\mu\text{m}$  PAH emission strength, we make the reasonable assumption that the profiles of the 3.3- $\mu\text{m}$  PAH emission in these LIRGs are similar to those of Galactic star-forming regions and nearby starburst galaxies (type-1 sources in Tokunaga et al. 1991), following Imanishi et al. (2006a). The adopted profile reproduces the observed 3.3- $\mu\text{m}$  PAH emission features of the LIRGs reasonably well. Table 8 summarizes the fluxes, luminosities, and rest-frame equivalent widths of the 3.3  $\mu\text{m}$  PAH emission feature. Only the equivalent width is not significantly affected by flux loss in our small-aperture spectra, and so will be used in our discussion.

#### 4.2.4. CO Absorption

Figure 10 shows enlarged spectra in the longer wavelength portion of the  $K$ -band spectra. All spectra show spectral gaps in the continuum at  $\lambda_{\text{obs}} > 2.35 \mu\text{m}$  in the observed frame. We attribute the gaps to CO absorption features at  $\lambda_{\text{rest}} = 2.31\text{--}2.4 \mu\text{m}$  produced by stars older than  $10^6 \text{ yr}$  (Oliva et al. 1999; Ivanov et al. 2000; Imanishi & Alonso-Herrero 2004; Imanishi & Wada 2004). To estimate the CO absorption strengths, we adopt the spectroscopic CO index ( $\text{CO}_{\text{spec}}$ ) defined by Doyon et al. (1994) and follow the procedures previously applied to other LIRGs by ourselves (Imanishi et al. 2004; Imanishi & Nakanishi 2006). Power-law continuum levels ( $F_{\lambda} = \alpha \times \lambda^{\beta}$ ), shown as solid lines in Fig. 10, are determined using data points at  $\lambda_{\text{rest}} = 2.05\text{--}2.29 \mu\text{m}$ , excluding obvious emission lines. The derived  $\text{CO}_{\text{spec}}$  values are summarized in column 5 of Table 8.

Ridgway et al. (1994) also estimated  $\text{CO}_{\text{spec}} = 0.24 \pm 0.03$  for NGC 2623, with a  $2''.7$  aperture, which agrees with our measurement of  $\text{CO}_{\text{spec}} = 0.27$  (Table 8) to within uncertainty. Goldader et al. (1997) measured the photometric CO index inside  $3'' \times 9''$  apertures and

estimated  $\text{CO}_{\text{ph}} = 0.23, 0.16,$  and  $0.18$  for NGC 2623, Mrk 266SW, and Arp 193, respectively. Using the formula  $\text{CO}_{\text{spec}} = 1.46 \times \text{CO}_{\text{ph}} - 0.02$  (Goldader et al. 1997), these  $\text{CO}_{\text{phot}}$  values are converted to  $\text{CO}_{\text{spec}} = 0.32, 0.21,$  and  $0.24$  for NGC 2623, Mrk 266SW, and Arp 193, respectively, which are slightly (0.02–0.05) larger than our measurements (Table 8).

## 5. DISCUSSION

### 5.1. Comparison of HCN(1–0)/HCO<sup>+</sup>(1–0)

#### Brightness-Temperature Ratios with Other Galaxies

Figure 11 plots the HCN(1–0)/HCO<sup>+</sup>(1–0) and HCN(1–0)/CO(1–0) brightness-temperature ratios for the four LIRGs. Previously obtained data points of nearby LIRGs (Imanishi et al. 2004, 2006b; Imanishi & Nakanishi 2006; Imanishi et al. 2007b), starbursts, and Seyfert galaxies (Kohno 2005) are also plotted. As stated by Imanishi et al. (2006b), the HCN(1–0)/HCO<sup>+</sup>(1–0) brightness-temperature ratios in the ordinate are mainly used in our discussions for the following reasons. First, since HCN(1–0) and HCO<sup>+</sup>(1–0) have similarly high dipole moments ( $\mu > 3$  debye; Botschwina et al. 1993; Millar et al. 1997), it is very likely that similar high-density molecular gas is probed with both lines. Next, as both the HCN(1–0) and HCO<sup>+</sup>(1–0) lines are observed simultaneously with the same NMA array configuration, their beam patterns are virtually identical. Finally, both HCN(1–0) and HCO<sup>+</sup>(1–0) fluxes are measured at the same time with the same receiver and same correlator unit, under the same weather conditions, so that possible *absolute* flux calibration uncertainties of interferometric data do not propagate to the ratio, which is dominated by statistical noise and fitting errors (see Fig. 7).

In Fig. 11, we note the following points: first, NGC 1377 exhibits a high HCN(1–0)/HCO<sup>+</sup>(1–0) brightness-temperature ratio, as seen in AGN-dominated galaxy nuclei. Second, the Mrk 266 NE nucleus shows a significantly higher ratio than the SW nucleus. Finally, the HCN(1–0)/HCO<sup>+</sup>(1–0) brightness-temperature ratios of Mrk 266 SW and Arp 193 are low, as observed in starburst galaxies, and that of NGC 2623 is higher than Mrk 266 SW and Arp 193.

### 5.2. Buried AGN Signatures in Individual Objects

In this subsection, we look for buried AGN signatures in the infrared spectra of individual LIRG nuclei and then investigate their HCN(1–0)/HCO<sup>+</sup>(1–0) brightness-temperature ratios. In doing so, we have to account for the fact that starburst activity surrounds the central compact buried AGN, so starburst emission is less obscured by gas and dust than the buried AGN emission. The contribution from the buried AGN to the observed infrared flux can be small, even if the buried AGN is intrinsically luminous and is energetically important, due to dust extinction. Thus, we need to examine the infrared spectra carefully.

#### 5.2.1. Mrk 266 NE

Although optical spectroscopy by various groups has failed to find AGN signatures in the Mrk 266 NE nucleus (Osterbrock & Dahari 1983; Kollatschny & Fricke 1984; Mazzarella & Boroson 1993; Wu et al. 1998; Goncalves et al. 1999; Ishigaki et al. 2000), buried AGN signatures are

discernible in our infrared spectra. First, Mrk 266 NE shows a high  $\text{H}_2(1-0) \text{ S}(1)$  to  $\text{Br}\gamma$  flux ratio,  $> 1$  (Table 7). Observationally, starburst galaxies show  $\text{H}_2(1-0) \text{ S}(1)$  to  $\text{Br}\gamma$  flux ratios of  $< 1$  (Mouri & Taniguchi 1992), while high  $\text{H}_2(1-0) \text{ S}(1)$  to  $\text{Br}\gamma$  flux ratios ( $> 1$ ) are found in optical AGNs (= Seyfert galaxies) (Mouri & Taniguchi 1992), as well as buried AGN candidates (Imanishi et al. 2004). Next, the rest-frame equivalent width of the  $3.3\text{-}\mu\text{m}$  PAH emission of Mrk 266 NE ( $\text{EW}_{3.3\text{PAH}} \sim 30 \text{ nm}$ ; Table 8) is significantly smaller than that observed in starburst galaxies ( $\sim 100 \text{ nm}$ ; Moorwood 1986; Imanishi & Dudley 2000), suggesting that a PAH-free AGN-heated hot dust continuum contributes significantly to the observed  $3\text{-}4 \mu\text{m}$  flux of Mrk 266 NE.

The  $\text{HCN}(1-0)/\text{HCO}^+(1-0)$  brightness-temperature ratio of Mrk 266 NE is also higher than that of the Mrk 266 SW nucleus. A putative buried AGN, suggested from X-ray data (Brassington et al. 2007), may enhance the  $\text{HCN}(1-0)$  emission in Mrk 266 NE.

### 5.2.2. NGC 1377

The  $\text{HCN}(1-0)/\text{HCO}^+(1-0)$  brightness-temperature ratio of NGC 1377 is high, as found in AGNs. The infrared  $L$ -band spectrum is also dominated by PAH-free continuum emission (Imanishi 2006), as usually seen in AGNs. The strong  $9.7 \mu\text{m}$  silicate dust absorption feature detected in the *Spitzer* IRS infrared  $5\text{-}35 \mu\text{m}$  spectrum (Roussel et al. 2006) is also incompatible with a normal starburst, where stellar energy sources and dust are spatially well mixed. It requires a buried AGN-type centrally concentrated energy source geometry (Imanishi et al. 2007a). These overall observational results are naturally explained by the presence of a luminous buried AGN in NGC 1377.

A PAH-free continuum and strong  $9.7\text{-}\mu\text{m}$  silicate dust absorption could be explained by an exceptionally centrally concentrated extreme starburst whose emitting volume is predominantly occupied with HII-regions, with virtually no molecular gas and photo-dissociation regions (Fig. 1e of Imanishi et al. 2007a). Unlike ULIRGs with  $L_{\text{IR}} > 10^{12} L_{\odot}$ , the absolute infrared luminosity of NGC 1377 is only  $\sim 10^{10.1} L_{\odot}$ , which could be accounted for by a small number of super star cluster whose emitting size is very small ( $\ll 100 \text{ pc}$ ) and emission surface brightness is high (Gorjian et al. 2001). In fact, Roussel et al. (2003) preferred such a compact starburst (super star cluster) scenario, but ruled out the possibility of an energetically important buried AGN, based on the following arguments: (1) estimated SMBH mass is too small to account for the luminosity of NGC 1377 with AGN activity, and (2) high excitation forbidden emission lines, usually seen in Seyfert galaxies, are not detected.

Regarding the first point, the SMBH mass was estimated to be  $< 2 \times 10^5 M_{\odot}$ , from the observed radio 20-cm (1.5-GHz) continuum flux and the small line width of the infrared  $\text{H}_2(1-0) \text{ S}(1)$  emission line (FWHM  $< 25 \text{ km s}^{-1}$ ) (Roussel et al. 2003). The measured line width of millimeter CO(1-0) lines in our NMA spectrum (Figure 6) is  $\sim 100 \text{ km s}^{-1}$  in FWHM. After correction for the velocity resolution of NMA data ( $\sim 42 \text{ km s}^{-1}$ ; §3.1), we obtain the intrinsic CO(1-0) line width of  $\sim 90 \text{ km s}^{-1}$  in FWHM, which is similar to the SEST 15-m telescope measurement (Roussel et al. 2003). Assuming the CO(1-0) line width and SMBH mass relation given by

Shields et al. (2006), the measured CO(1-0) line width provides a similar SMBH mass of  $\sim 2 \times 10^5 M_{\odot}$ . The Eddington luminosity of this SMBH mass is  $\sim 7 \times 10^9 L_{\odot}$ . This is only slightly below the observed infrared luminosity ( $\sim 1 \times 10^{10} L_{\odot}$ ). In a buried AGN, the infrared luminosity should be comparable to the bolometric luminosity, because almost all of the energetic radiation from the central AGN is absorbed by the surrounding dust and re-emitted as infrared thermal dust emission. Thus, even if current constraints on the supermassive black hole mass are accurate, it is still possible that the bulk of the observed luminosity in NGC 1377 comes from buried AGN activity.

However, uncertainties in the estimated SMBH mass in NGC 1377 could exist. First, the observed 20-cm flux from a buried AGN can be severely attenuated by free-free absorption, possibly leading to an underestimate of the SMBH mass. Second, the line width of  $\text{H}_2(1-0) \text{ S}(1)$  emission is not well calibrated for an SMBH mass estimate. Finally, in the small line width range of millimeter CO(1-0) ( $< 100 \text{ km s}^{-1}$ ), the SMBH mass estimated from CO(1-0) line width yields systematically smaller results than other measurements (Shields et al. 2006). Hence, the actual SMBH mass in NGC 1377 could be higher than above estimates.

Regarding the second point, the non-detection of high excitation emission lines is a natural consequence of a buried AGN because the central AGN is obscured by dust and gas along virtually all directions at the inner part ( $< 1 \text{ pc}$ ), producing virtually no narrow line regions (= the main emitting sources of high excitation lines).

Therefore, none of the currently available observational results preclude the presence of a luminous buried AGN in NGC 1377. Strong  $\text{H}_2$  emission is observed in NGC 1377 (Roussel et al. 2006). In general,  $\text{H}_2$  emission is stronger in AGNs than starburst galaxies (Mouri & Taniguchi 1992). Although a major galaxy merger could produce strong  $\text{H}_2$  emission (Van der Werf et al. 1993), NGC 1377 shows no sign of a major merger (Roussel et al. 2006). Energy source obscuration for NGC 1377 is extremely high (Roussel et al. 2006), and the observed low radio to infrared luminosity ratio (Roussel et al. 2003) could be explained by severe flux attenuation of the radio 20-cm (1.5 GHz) emission by free-free absorption.

### 5.2.3. NGC 2623

The  $\text{EW}_{3.3\text{PAH}}$  and  $\text{CO}_{\text{spec}}$  values, and the  $\text{H}_2(1-0) \text{ S}(1)$  to  $\text{Br}\gamma$  flux ratio of NGC 2623 are all within starburst range. The  $\text{HCN}(1-0)/\text{HCO}^+(1-0)$  brightness-temperature ratios are slightly higher than Arp 193 and Mrk 266 SW, which may be due to an  $\text{HCN}(1-0)$  emission enhancement by an X-ray detected buried AGN (see §2).

### 5.2.4. Mrk 266 SW and Arp 193

The large  $\text{EW}_{3.3\text{PAH}}$  and  $\text{CO}_{\text{spec}}$  values, the small  $\text{H}_2(1-0) \text{ S}(1)$  to  $\text{Br}\gamma$  flux ratios, and the small  $\text{HCN}(1-0)/\text{HCO}^+(1-0)$  brightness-temperature ratios of Mrk 266 SW and Arp 193 are all explained by starburst activity only, with no significant AGN contribution required.

## 5.3. Interpretation of High $\text{HCN}(1-0)/\text{HCO}^+(1-0)$ Brightness-Temperature Ratios in Buried AGN Candidates

One natural explanation for the high HCN(1–0)/HCO<sup>+</sup>(1–0) brightness-temperature ratios found in AGNs is an HCN abundance enhancement. If molecular gas consists of small dense gas clumps with low volume filling factor, as widely supported from observations (Solomon et al. 1987), an enhanced HCN abundance can result in higher HCN(1–0) flux regardless of whether the HCN(1–0) emission is optically thin or thick (Imanishi et al. 2007b). Several chemical calculations of HCN abundance in molecular gas around UV- and X-ray emitting energy sources have been published (Meijerink et al. 2006; Lintott & Viti 2006). Although an HCN abundance enhancement around an X-ray emitting energy source (i.e., AGN) is predicted in some parameter ranges that are realistic for molecular gas around buried AGNs in LIRGs (high-F<sub>X</sub> range of Table 3 in Meijerink et al. 2006), an HCN abundance *decrease* is suggested in other reasonable parameter ranges (Meijerink et al. 2006). The chemical calculation results are highly dependent on parameters, and it is currently unclear whether an HCN abundance is indeed enhanced in molecular gas in the close vicinity of buried AGNs in LIRG nuclei.

The second possible explanation for the strong HCN(1–0) emission in AGNs is an infrared radiative pumping scenario (Aalto et al. 1995; Garcia-Burillo et al. 2006; Weiss et al. 2007). It is usually assumed that molecular gas is excited by collision. However, the HCN molecule has a line at infrared 14  $\mu\text{m}$  that can be excited by absorbing photons at  $\lambda \sim 14 \mu\text{m}$ . HCN(1–0) emission in the millimeter wavelength range could be enhanced through a cascade process. Since the emission surface brightness of an AGN is high, much of the surrounding dust is heated to several 100 K, producing strong mid-infrared 10–20  $\mu\text{m}$  emission (§1). Hence, this infrared radiative pumping scenario for HCN could work effectively in AGNs.

HCO<sup>+</sup> also has a line at infrared 12  $\mu\text{m}$ , so that the infrared radiative pumping mechanism could work in a similar way. Observationally, the 14  $\mu\text{m}$  HCN absorption features are detected in highly obscured LIRGs (Lahuis et al. 2007), but the 12  $\mu\text{m}$  HCO<sup>+</sup> absorption features are not (Farrah et al. 2007). It may be that this infrared radiative pumping scenario is working more effectively for HCN than HCO<sup>+</sup>, possibly enhancing the HCN(1–0)/HCO<sup>+</sup>(1–0) brightness-temperature ratios in AGNs.

To test this infrared radiative pumping scenario, in Figure 12 we compare the observed HCN(1–0)/HCO<sup>+</sup>(1–0) brightness-temperature ratio with the infrared emission surface brightness estimated by Soifer et al. (2000, 2001) and Evans et al. (2003). We use the infrared emission surface brightness, rather than infrared luminosity (Gracia-Carpio et al. 2006), because the bulk of the observed normal LIRGs with  $<10^{12}L_{\odot}$  (i.e., non-ULIRGs) are chosen because they display luminous buried AGN signatures. Although Gracia-Carpio et al. (2008) found an increasing trend of HCN(1–0)/HCO<sup>+</sup>(1–0) brightness-temperature ratios with increasing galaxy infrared luminosities, our heterogeneous sample selection of normal LIRGs (non-ULIRGs) could be biased to AGN candidates (= strong HCN emitters) and artificially eliminate this trend. The infrared radiative pumping scenario can, in principle, enhance the HCN(1–0)/HCO<sup>+</sup>(1–

0) brightness-temperature ratio, even for a low absolute infrared luminosity galaxy (e.g. NGC 1377), if infrared emission surface brightness is high.

In Fig. 12, we may see a weak correlation but the scatter is large and the total sample size is small. Based on our current dataset, we cannot determine whether the infrared radiative pumping scenario is indeed at work in buried AGNs at LIRG’s nuclei. Further detailed theoretical calculations that realistically incorporate the actual energy level populations of HCN and HCO<sup>+</sup>, as well as the clumpy structure of molecular gas around an AGN (Yamada et al. 2007), are needed to properly interpret the origin of strong HCN(1–0) emission in AGNs. Combination with higher transition lines in the submillimeter wavelength range (Wilson et al. 2008) will also help better understand the physical properties of molecular gas in LIRG’s nuclei.

## 6. SUMMARY

We presented the results of millimeter interferometric simultaneous HCN(1–0) and HCO<sup>+</sup>(1–0) observations of four LIRGs using NMA. When combined with previously observed LIRGs, ours is the largest LIRG interferometric HCN(1–0) and HCO<sup>+</sup>(1–0) survey. From our interferometric data, we extracted the HCN(1–0) and HCO<sup>+</sup>(1–0) fluxes at the nuclei, where putative AGNs are expected to be present. We derived the HCN(1–0)/HCO<sup>+</sup>(1–0) brightness-temperature ratios of the observed LIRG nuclei and compared them with the ratios found in AGNs and starburst galaxies. The main result of this paper is the confirmation of the previously discovered trend that LIRGs with luminous buried AGN signatures at other wavelengths tend to show higher HCN(1–0)/HCO<sup>+</sup>(1–0) brightness-temperature ratios than those without. This reinforces the utility of the HCN(1–0)/HCO<sup>+</sup>(1–0) brightness-temperature ratio as a powerful observational tool for discovering elusive AGNs deeply buried in dust and molecular gas.

We are grateful to the NRO staff for their continuous efforts to make our NMA observations possible. We also thank D. Griep for his support during our IRTF observing runs, and the anonymous referee for his/her useful comments. M.I. is supported by Grants-in-Aid for Scientific Research (19740109). Y.T. is financially supported by the Japan Society for the Promotion of Science (JSPS) for Young Scientists. NRO is a branch of the National Astronomical Observatory, National Institutes of Natural Sciences, Japan. This study utilized the SIMBAD database, operated at CDS, Strasbourg, France, and the NASA/IPAC Extragalactic Database (NED) operated by the Jet Propulsion Laboratory, California Institute of Technology, under contract with the National Aeronautics and Space Administration. This publication makes use of data products from the Two Micron All Sky Survey, which is a joint project of the University of Massachusetts and the Infrared Processing and Analysis Center/California Institute of Technology, funded by the National Aeronautics and Space Administration and the National Science Foundation.

## REFERENCES

- Aalto, S., Booth, R. S., Black, J. H., & Johansson, L. E. B. 1995, A&A, 300, 369
- Aalto, S., Spaans, M., Wiedner, M. C., & Huttemeister, S. 2007, A&A, 464, 193

- Botschwina, P., Horn, M., Flugge, J., Seeger, S. 1993, *J. Chem. Soc. Faraday Trans.*, 89, 2219
- Brassington, N. J., Ponman, T. J., & Read, M. 2007, *MNRAS*, 377, 1439
- Brandl, B. et al. 2006, *ApJ*, 653, 1129
- Bryant, P. M., & Scoville, N. Z. 1999, *AJ*, 117, 2632
- Carico, D. P., Sanders, D. B., Soifer, B. T., Matthews, K., & Neugebauer, G. 1990, *AJ*, 100, 70
- Condon, J. J., Huang, Z. -P., Yin, Q. F., & Thuan, T. X. 1991, *ApJ*, 378, 65
- Downes, D., & Solomon, P. M. 1998, *ApJ*, 507, 615
- Doyon, R., Joseph, R. D., & Wright, G. S. 1994, *ApJ*, 421, 101
- Evans, A. S. et al. 2003, *AJ*, 125, 2341
- Evans, A. S. et al. 2008, *ApJ*, 675, L69
- Fabian, A. C., Wilman, R. J., & Crawford, C. S., 2002, *MNRAS*, 329, L18
- Farrah, D. et al. 2007, *ApJ*, 667, 149
- Gao, Y., & Solomon, P. M. 2004, *ApJS*, 152, 63
- Garcia-Burillo, S., et al. 2006, *ApJ*, 645, L17
- Goldader, J. D., Joseph, R. D., Doyon, R., & Sanders, D. B. 1997, *ApJS*, 108, 449
- Goncalves, A. C., Veron-Cetty, M. -P., & Veron, P. 1999, *A&AS*, 135, 437
- Gorjian, V., Turner, J. L., & Beck, S. C. 2001, *ApJ*, 554, L29
- Gracia-Carpio, J., Garcia-Burillo, S., Planesas, P., & Colina, L. 2006, *ApJ*, 640, L135
- Gracia-Carpio, J., Garcia-Burillo, S., Planesas, P., Fuente, A., & Usero, A. 2008, *A&A*, 479, 703
- Guelin, M., et al. 2007, *A&A*, 462, L45
- Hill, G. J., Goodrich, R. W., & Depoy, D. L. 1996, *ApJ*, 462, 163
- Imanishi, M. 2002, *ApJ*, 569, 44
- Imanishi, M. 2006, *AJ*, 131, 2406
- Imanishi, M., & Alonso-Herrero, A. 2004, *ApJ*, 614, 122
- Imanishi, M., & Dudley, C. C. 2000, *ApJ*, 545, 701
- Imanishi, M., & Maloney, P. R. 2003, *ApJ*, 588, 165
- Imanishi, M., & Nakanishi, K. 2006, *PASJ*, 58, 813
- Imanishi, M., & Wada, K., 2004, *ApJ*, 617, 214
- Imanishi, M., Dudley, C. C., & Maloney, P. R. 2006a, *ApJ*, 637, 114
- Imanishi, M., Dudley, C. C., Maiolino, R., Maloney, P. R., Nakagawa, T., & Risaliti, G. 2007a, *ApJS*, 171, 72
- Imanishi, M., Nakagawa, T., Ohshima, Y., Shirahata, M., Wada, T., Onaka, T., & Oi, N. 2008, *PASJ*, in press (ArXiv:0808:0363)
- Imanishi, M., Nakanishi, K., Kuno, N., & Kohno, K. 2004, *AJ*, 128, 2037
- Imanishi, M., Nakanishi, K., & Kohno, K. 2006b, *AJ*, 131, 2888
- Imanishi, M., Nakanishi, K., Tamura, Y., Oi, N., & Kohno, K. 2007b, *AJ*, 134, 2366
- Ishigaki, T. et al. 2000, *PASJ*, 52, 185
- Ivanov, V. D., Rieke, G. H., Groppi, C. E., Alonso-Herrero, A., Rieke, M. J., & Engelbracht, C. W. 2000, *ApJ*, 545, 190
- Keel, W. C. 1984, *ApJ*, 282, 75
- Kenney, J. D., & Young, J. S. 1988, *ApJS*, 66, 162
- Kim, D. -C., Sanders, D. B., Veilleux, S., Mazzarella, J. M., & Soifer, B. T. 1995, *ApJS*, 98, 129
- Kohno, K. 2005, in *AIP Conf. Ser.* 783, *The Evolution of Starbursts*, ed. S. Hüttemeister, E. Manthey, D. Bomans, & K. Weis (New York: AIP), 203 (astro-ph/0508420)
- Kohno, K., Matsushita, S., Vila-Vilaro, B., Okumura, S. K., Shibatsuka, T., Okiura, M., Ishizuki, S., Kawabe, R. 2001, in *ASP Conf. Ser.* 249, *The Central kpc of Starbursts and AGN*, ed. J. H. Knapen, J. E., Beckman, I. Shlosman, & T. J. Mahoney (San Francisco: ASP), 672 (astro-ph/0206398)
- Kollatschny, W., & Fricke, K. J. 1984, *A&A*, 135, 171
- Krips, M., Neri, R., Garcia-Burillo, S., Martin, S., Combes, F., Gracia-Carpio, J., & Eckart, A. 2008, *ApJ*, 677, 262
- Lahuis, F. et al. 2007, *ApJ*, 659, 296
- Lintott, C., & Viti, S. 2006, *ApJ*, 646, L37
- Lutz, D., Maiolino, R., Moorwood, A. F. M., Netzer, H., Wagner, S. J., Sturm, E., & Genzel, R. 2002, *A&A*, 396, 439
- Maiolino, R. et al. 2003, *MNRAS*, 344, L59
- Mazzarella, J. M., & Boroson, T. A. 1993, *ApJS*, 85, 27
- Meijerink, R. Spaans, M., & Israel, F. P. 2006, *ApJ*, 650, L103
- Millar, T. J., Farquhar, P. R. A., & Willacy, K. 1997, *A&AS*, 121, 139
- Moorwood, A. F. M. 1986, *A&A*, 166, 4
- Mouri, H., & Taniguchi, Y. 1992, *ApJ*, 386, 68
- Okumura, S. et al. 2000, *PASJ*, 52, 393
- Oliva, E., Origlia, L., Maiolino, R., & Moorwood, A. F. M. 1999, *A&A*, 350, 9
- Osterbrock, D. E., & Dahari, O. 1983, *ApJ*, 273, 478
- Papadopoulos, P. P. 2007, *ApJ*, 656, 792
- Rayner, J. T., Toomey, D. W., Onaka, P. M., Denault, A. J., Stahlberger, W. E., Vacca, W. D., Cushing, M. C., & Wang, S. 2003, *PASP*, 115, 362
- Ridgway, S. E., Wynn-Williams, C. G., & Becklin, E. E. 1994, *ApJ*, 428, 609
- Rothberg, B., & Joseph, R. D. 2004, *AJ*, 128, 2098
- Roussel, H., Helou, G., Beck, R., Condon, J. J., Bosma, A., Matthews, K., & Jarrett, T. H. 2003, *ApJ*, 593, 733
- Roussel, H., et al. 2006, *ApJ*, 646, 841
- Sanders, D. B., & Mirabel, I. F. 1996, *ARA&A*, 34, 749
- Sanders, D. B., Scoville, N. Z., Young, J. S., Soifer, B. T., Schloerb, F. P., Rice, W. L., & Danielson, G. E. 1986, *ApJ*, 305, L45
- Sanders, D. B., Soifer, B. T., Elias, J. H., Madore, B. F., Matthews, K., Neugebauer, G., & Scoville, N. Z. 1988a, *ApJ*, 325, 74
- Sanders, D. B., Soifer, B. T., Elias, J. H., Neugebauer, G., & Matthews, K. 1988b, *ApJ*, 328, L35
- Shields, G. A., Menezes, K. L., Massart, C. A., & Vanden Bout, P. 2006, *ApJ*, 641, 683
- Skrutskie, M. F., et al. 2006, *AJ*, 131, 1163
- Soifer, B. T. et al. 2000, *AJ*, 119, 509
- Soifer, B. T. et al. 2001, *AJ*, 122, 1213
- Solomon, P. M., Downes, D., & Radford, S. J. E. 1992, *ApJ*, 387, L55
- Solomon, P. M., Rivolo, A. R., Barrett, J., & Yahil, A. 1987, *ApJ*, 319, 730
- Thompson, T. A., Quataert, E., & Murray, N. 2005, *ApJ*, 630, 167
- Thorne, K. S. 1974, *ApJ*, 191, 507
- Tokunaga, A. T. 2000, in *Allen's Astrophysical Quantities*, ed. A. N. Cox (4th ed; Berlin: Springer), 143
- Tokunaga A. T., Sellgren K., Smith R. G., Nagata T., Sakata A., Nakada Y., 1991, *ApJ*, 380, 452
- Tsutsumi, T. Morita, K. -I. & Umeyama, S. 1997, in *Astronomical Data Analysis Software and Systems VI*, ed. G. Hunt, & H. E. Payne (San Francisco: ASP), 50
- Van der Werf, P. P., Genzel, R., Krabbe, A., Blietz, M., Lutz, D., Drapatz, B., Ward, M. J., & Forbes, D. A., 1993, *ApJ*, 405, 522
- Vega, O., Clemens, M. S., Bressan, A., Granato, G. L., Silva, L., & Panuzzo, P. 2008, *A&A*, 484, 631
- Veilleux, S., Goodrich, R. W., & Hill, G. J. 1997, *ApJ*, 477, 631
- Veilleux, S., Kim, D. -C., Sanders, D. B., Mazzarella, J. M., & Soifer, B. T. 1995, *ApJS*, 98, 171
- Veilleux, S., & Osterbrock, D. E. 1987, *ApJS*, 63, 295
- Weiss, A., Downes, D., Neri, R., Walter, F., Henkel, C., Wilner, D. J., Wagg, J., & Wiklind, T. 2007, *A&A*, 467, 955
- Wilson, C. D., et al. 2008, *ApJ*, 178, 189
- Wu, H., Zou, Z. L., Xia, X. Y., & Deng, Z. G. 1998, *A&A*, 132, 181
- Yamada, M., Wada, K., & Tomisaka, K. 2007, *ApJ*, 671, 73

TABLE 1  
DETAILED INFORMATION ON THE OBSERVED LIRGS

| Object                     | Redshift | $f_{12}$<br>(Jy) | $f_{25}$<br>(Jy) | $f_{60}$<br>(Jy) | $f_{100}$<br>(Jy) | $\log L_{\text{IR}}$ ( $\log L_{\text{IR}}/L_{\odot}$ )<br>(ergs s <sup>-1</sup> ) | Far-infrared<br>Color |
|----------------------------|----------|------------------|------------------|------------------|-------------------|--|-----------------------|
| (1)                        | (2)      | (3)              | (4)              | (5)              | (6)               | (7)  | (8)                   |
| NGC 2623 (Arp 243)         | 0.018    | 0.21             | 1.74             | 23.13            | 27.88             | 45.1 (11.5)  | 0.08 (cool)           |
| Mrk 266 (NGC 5256)         | 0.028    | 0.23             | 0.98             | 7.34             | 11.07             | 45.0 (11.5)  | 0.13 (cool)           |
| Arp 193 (IC 883, UGC 8387) | 0.023    | 0.26             | 1.36             | 15.44            | 25.18             | 45.2 (11.6)  | 0.09 (cool)           |
| NGC 1377                   | 0.006    | 0.44             | 1.81             | 7.25             | 5.74              | 43.7 (10.1)  | 0.25 (warm)           |

NOTE. — Col.(1): Object name. Col.(2): Redshift. Cols.(3)–(6):  $f_{12}$ ,  $f_{25}$ ,  $f_{60}$ , and  $f_{100}$  are *IRAS FSC* fluxes at 12, 25, 60, and 100  $\mu\text{m}$ , respectively. Col.(7): Decimal logarithm of the infrared (8–1000  $\mu\text{m}$ ) luminosity in ergs s<sup>-1</sup> calculated as follows:  $L_{\text{IR}} = 2.1 \times 10^{39} \times D(\text{Mpc})^2 \times (13.48 \times f_{12} + 5.16 \times f_{25} + 2.58 \times f_{60} + f_{100})$  ergs s<sup>-1</sup> (Sanders & Mirabel 1996). The values in parentheses are the decimal logarithms of the infrared luminosities in units of solar luminosities. Col.(8): *IRAS* 25  $\mu\text{m}$  to 60  $\mu\text{m}$  flux ratio ( $f_{25}/f_{60}$ ). LIRGs with  $f_{25}/f_{60} < (>) 0.2$  are classified as cool (warm) (Sanders et al. 1988b).

TABLE 2  
OBSERVING LOG OF NMA MILLIMETER INTERFEROMETRIC OBSERVATIONS

| Object   | Array<br>configuration | Observing Date<br>(UT)          | Central<br>frequency | Phase<br>calibrator | Band-pass<br>calibrator | Flux<br>calibrator |
|----------|------------------------|---------------------------------|----------------------|---------------------|-------------------------|--------------------|
| (1)      | (2)                    | (3)                             | (4)                  | (5)                 | (6)                     | (7)                |
| NGC 2623 | C                      | 2007 Dec 13, 14, 15, 16         | 87.30                | 0851+202            | 3C 84                   | 3C 345             |
| Mrk 266  | C                      | 2008 Jan 8, 9, 10               | 86.52                | 1418+546            | 3C 84                   | 1749+096           |
|          | D                      | 2008 Feb 20, 21, 22, Mar 4, 5   |                      |                     |                         |                    |
|          | C (CO)                 | 2007 Dec 19, 23                 | 112.43               | 1418+546            | 3C 84                   | 1749+096           |
| Arp 193  | C                      | 2007 Dec 20                     | 86.89                | 1308+326            | 3C 84                   | 1749+096           |
|          | D                      | 2008 Feb 18, 19                 |                      |                     |                         |                    |
| NGC 1377 | D                      | 2006 Dec 12, 13                 | 88.47                | 0420–014            | 3C 454.3                | Uranus             |
|          | AB                     | 2007 Jan 27, 28                 |                      |                     |                         |                    |
|          | C                      | 2007 Dec 13, 14, 15, 16, 19, 20 |                      |                     |                         |                    |
|          | C (CO)                 | 2007 Dec 10, 11                 | 114.95               | 0420–014            | 3C 454.3                | Uranus             |

NOTE. — Col.(1): Object name. Col.(2): NMA array configuration. The mark “(CO)” means CO(1–0) observations, which were executed only for Mrk 266 and NGC 1377. Col.(3): Observing date in UT. Col.(4): Central frequency used for the observations. Col.(5): Object name used as a phase calibrator. Col.(6): Object name used as a band-pass calibrator. Col.(7): Object name used as a flux calibrator.

TABLE 3  
PARAMETERS OF FINAL NMA MAPS

| Object   | Line                 | On source<br>integration (hr) | Beam size<br>(arcsec $\times$ arcsec) | Position angle of<br>the beam ( $^{\circ}$ ) |
|----------|----------------------|-------------------------------|---------------------------------------|--|
| (1)      | (2)                  | (3)                           | (4)                                   | (5)  |
| NGC 2623 | HCN/HCO <sup>+</sup> | 10                            | 5.4 $\times$ 4.2                      | –48.4  |
| Mrk 266  | HCN/HCO <sup>+</sup> | 34                            | 4.3 $\times$ 3.4                      | –31.5  |
|          | CO                   | 5                             | 4.3 $\times$ 3.4                      | –31.5  |
| Arp 193  | HCN/HCO <sup>+</sup> | 8                             | 7.1 $\times$ 6.6                      | –52.5  |
| NGC 1377 | HCN/HCO <sup>+</sup> | 23                            | 7.1 $\times$ 4.0                      | –13.6  |
|          | CO                   | 4                             | 6.7 $\times$ 3.6                      | –18.8  |

NOTE. — Col.(1): Object name. Col.(2): Observed line. HCN(1–0)/HCO<sup>+</sup>(1–0) or CO(1–0). Col.(3): Net on-source integration time in hours. Col.(4): Beam size in arcsec  $\times$  arcsec. Col.(5): Position angle of the beam pattern. It is 0 $^{\circ}$  for the north-south direction, and increases counterclockwise on the sky plane.

TABLE 4  
OBSERVING LOG OF INFRARED SPECTROSCOPY WITH IRTF SPEX

| Object     | Date<br>(UT)  | Integration<br>(Min) | Name    | Standard Stars  |                 | Type    | $T_{\text{eff}}$ (K) |
|------------|---------------|----------------------|---------|-----------------|-----------------|---------|----------------------|
| (1)        | (2)           | (3)                  | (4)     | $K$ -mag<br>(5) | $L$ -mag<br>(6) | (7)     | (8)                  |
| NGC 2623   | 2008 April 20 | 60                   | HR 3262 | 3.9             | 3.9             | F6V     | 6400                 |
| Mrk 266 SW | 2008 April 19 | 40                   | HR 4767 | 4.9             | 4.8             | F9V-G0V | 6000                 |
| Mrk 266 NE | 2008 April 19 | 60                   | HR 4767 | 4.9             | 4.8             | F9V-G0V | 6000                 |
| Arp 193    | 2008 April 20 | 60                   | HR 4845 | 4.5             | 4.5             | G0V     | 5930                 |

NOTE. — Column (1): Object name. Col.(2): Observing date in UT. Col.(3): Net on-source integration time in min. Col.(4): Standard star name. Col.(5): Adopted  $K$ -band magnitude. Col.(6): Adopted  $L$ -band magnitude. Col.(7): Stellar spectral type. Col.(8): Effective temperature.

TABLE 5  
GAUSSIAN FITTING PARAMETERS AND NUCLEAR FLUXES OF HCN(1-0), HCO+(1-0), AND CO(1-0) EMISSION LINES

| Object<br>(1) | LSR velocity<br>[km s <sup>-1</sup> ] |                  |                | Flux<br>[Jy km s <sup>-1</sup> ] |                  |                | HCN(1-0)/HCO+(1-0)<br>Ratio<br>(8) |
|---------------|---------------------------------------|------------------|----------------|----------------------------------|------------------|----------------|------------------------------------|
|               | HCN(1-0)<br>(2)                       | HCO+(1-0)<br>(3) | CO(1-0)<br>(4) | HCN(1-0)<br>(5)                  | HCO+(1-0)<br>(6) | CO(1-0)<br>(7) |                                    |
| NGC 2623      | 5570                                  | 5620             | ...            | 5.8                              | 4.0              | 153            | 1.5                                |
| Mrk 266 SW    | 8290                                  | 8290             | 8370           | 1.0                              | 3.5              | 88             | 0.3                                |
| Mrk 266 NE    | 8330                                  | 8370             | 8250 + 8501    | 1.1                              | 0.8              | 18             | 1.4                                |
| Arp 193       | 6905 + 7110                           | 6850 + 7130      | ...            | 10.8                             | 12.7             | 202            | 0.9                                |
| NGC 1377      | 1500                                  | ...              | 1740           | 2.2                              | <1.2             | 9.6            | >1.8                               |

NOTE. — Col.(1): Object name. Cols.(2)–(4): LSR velocity  $\{v_{\text{opt}} \equiv (\frac{v_0}{v} - 1) \times c\}$  of the HCN(1-0), HCO+(1-0), and CO(1-0) in [km s<sup>-1</sup>]. Cols.(5)–(7): Flux of the HCN(1-0), HCO+(1-0), and CO(1-0) in [Jy km s<sup>-1</sup>] at the nuclear peak position. For NGC 2623 and Arp 193, the CO(1-0) fluxes are adopted from Bryant & Scoville (1999). Col.(8): HCN(1-0)/HCO+(1-0) ratio in brightness temperature ( $\propto \lambda^2 \times \text{flux density}$ ). The ratio is not affected by possible absolute flux calibration uncertainties in the NMA data (see §5.1).

TABLE 6  
COMPARISON OF HCN(1–0), HCO<sup>+</sup>(1–0), AND CO(1–0) FLUX BETWEEN OUR  
NMA INTERFEROMETRIC MEASUREMENTS AND SINGLE-DISH TELESCOPE’S  
MEASUREMENTS IN THE LITERATURE

| Nucleus<br>(1) | Line<br>(2)            | Flux<br>(3)                | Reference<br>(4)            |
|----------------|------------------------|----------------------------|-----------------------------|
| Mrk 266        | CO(1–0)                | 180 (SW + NE) <sup>a</sup> | This work                   |
|                |                        | 206 <sup>b</sup>           | Sanders et al. (1986)       |
| Arp 193        | HCN(1–0)               | 10.8                       | This work                   |
|                |                        | 25 <sup>c</sup>            | Solomon et al. (1992)       |
|                |                        | 6.3 <sup>d</sup>           | Gracia-Carpio et al. (2008) |
|                |                        | 12.7                       | This work                   |
|                | HCO <sup>+</sup> (1–0) | 10.0 <sup>d</sup>          | Gracia-Carpio et al. (2008) |
| NGC 1377       | CO(1–0)                | 9.6                        | This work                   |
|                |                        | 47 <sup>e</sup>            | Roussel et al. (2003)       |

NOTE. — Col.(1): Object name. Col.(2): HCN(1–0), HCO<sup>+</sup>(1–0), or CO(1–0) line. Col.(3): Flux in [Jy km s<sup>−1</sup>]. Col.(4): Reference.

<sup>a</sup>For the CO(1–0) flux from the SW nucleus, we adopt the total flux of 162 Jy km s<sup>−1</sup> (§4.1), as the spatially-extended component is very strong.

<sup>b</sup>A conversion factor of 42 Jy K<sup>−1</sup> is assumed for FCRAO 14-m telescope (Kenny & Young 1988).

<sup>c</sup>A conversion factor of 4.4 Jy K<sup>−1</sup> is assumed for IRAM 30-m telescope (Solomon et al. 1992).

<sup>d</sup>A conversion factor of 6.0 Jy K<sup>−1</sup> (“K” is antenna temperature in this case) is assumed for IRAM 30-m telescope (Gracia-Carpio et al. 2008).

<sup>e</sup>A conversion factor of 27 Jy K<sup>−1</sup> is assumed for SEST 15-m telescope at 115 GHz (<http://www.ls.eso.org/lasilla/Telescopes/SEST/html/telescope-instruments/telescope/index.html>).

TABLE 7  
PROPERTIES OF HYDROGEN EMISSION LINES

| Object<br>(1) | Pa $\alpha$ |             | Br $\alpha$ |             | Br $\gamma$ | H <sub>2</sub> | Pa $\alpha$ /Br $\alpha$<br>(8) | H <sub>2</sub> /Br $\gamma$<br>(9) |
|---------------|-------------|-------------|-------------|-------------|-------------|----------------|---------------------------------|------------------------------------|
|               | flux<br>(2) | FWHM<br>(3) | flux<br>(4) | FWHM<br>(5) | flux<br>(6) | flux<br>(7)    |                                 |                                    |
| NGC 2623      | 92          | 515         | 40          | 510         | 8           | 6.5            | 2.5                             | 0.8                                |
| Mrk 266 SW    | 40          | 365         | ...         | ...         | 7           | 2.5            | ...                             | 0.3                                |
| Mrk 266 NE    | 50          | 510         | ...         | ...         | 2           | 7              | ...                             | 3.5                                |
| Arp 193       | 72          | 440         | 39          | 465         | 11          | 7.5            | 2                               | 0.7                                |

NOTE. — Col.(1): Object name. Col.(2): Pa $\alpha$  flux in [10<sup>−15</sup> ergs s<sup>−1</sup> cm<sup>−2</sup>]. Col.(3): Pa $\alpha$  line width in FWHM in [km s<sup>−1</sup>]. Col.(4): Br $\alpha$  flux in [10<sup>−15</sup> ergs s<sup>−1</sup> cm<sup>−2</sup>]. Col.(5): Br $\alpha$  line width in FWHM in [km s<sup>−1</sup>]. Col.(6): Br $\gamma$  flux in [10<sup>−15</sup> ergs s<sup>−1</sup> cm<sup>−2</sup>]. Col.(7): H<sub>2</sub>(1–0) S(1) flux in [10<sup>−15</sup> ergs s<sup>−1</sup> cm<sup>−2</sup>]. Col.(8): Pa $\alpha$ /Br $\alpha$  flux ratio. Col.(9): H<sub>2</sub>/Br $\gamma$  flux ratio.

TABLE 8  
 PROPERTIES OF 3.3- $\mu\text{M}$  PAH EMISSION AND 2.3- $\mu\text{M}$  CO  
 ABSORPTION

| Object<br>(1) | $f_{3.3\text{PAH}}$<br>(2) | $L_{3.3\text{PAH}}$<br>(3) | $\text{EW}_{3.3\text{PAH}}$<br>(4) | $\text{CO}_{\text{spec}}$<br>(5) |
|---------------|----------------------------|----------------------------|------------------------------------|----------------------------------|
| NGC 2623      | 16                         | 1.0                        | 125                                | 0.27                             |
| Mrk 266 SW    | 9                          | 1.4                        | 70                                 | 0.19                             |
| Mrk 266 NE    | 3                          | 0.4                        | 30                                 | 0.24                             |
| Arp 193       | 21                         | 2.2                        | 140                                | 0.21                             |

NOTE. — Col.(1): Object name. Col.(2): Observed flux of 3.3- $\mu\text{m}$  PAH emission in [ $10^{-14}$  ergs  $\text{s}^{-1} \text{cm}^{-2}$ ]. Col.(3): Observed luminosity of 3.3- $\mu\text{m}$  PAH emission in [ $10^{41}$  ergs  $\text{s}^{-1}$ ]. Col.(4): Rest-frame equivalent width of the 3.3- $\mu\text{m}$  PAH emission in [nm]. Col.(5): Spectroscopic CO index defined by Doyon et al. (1994).

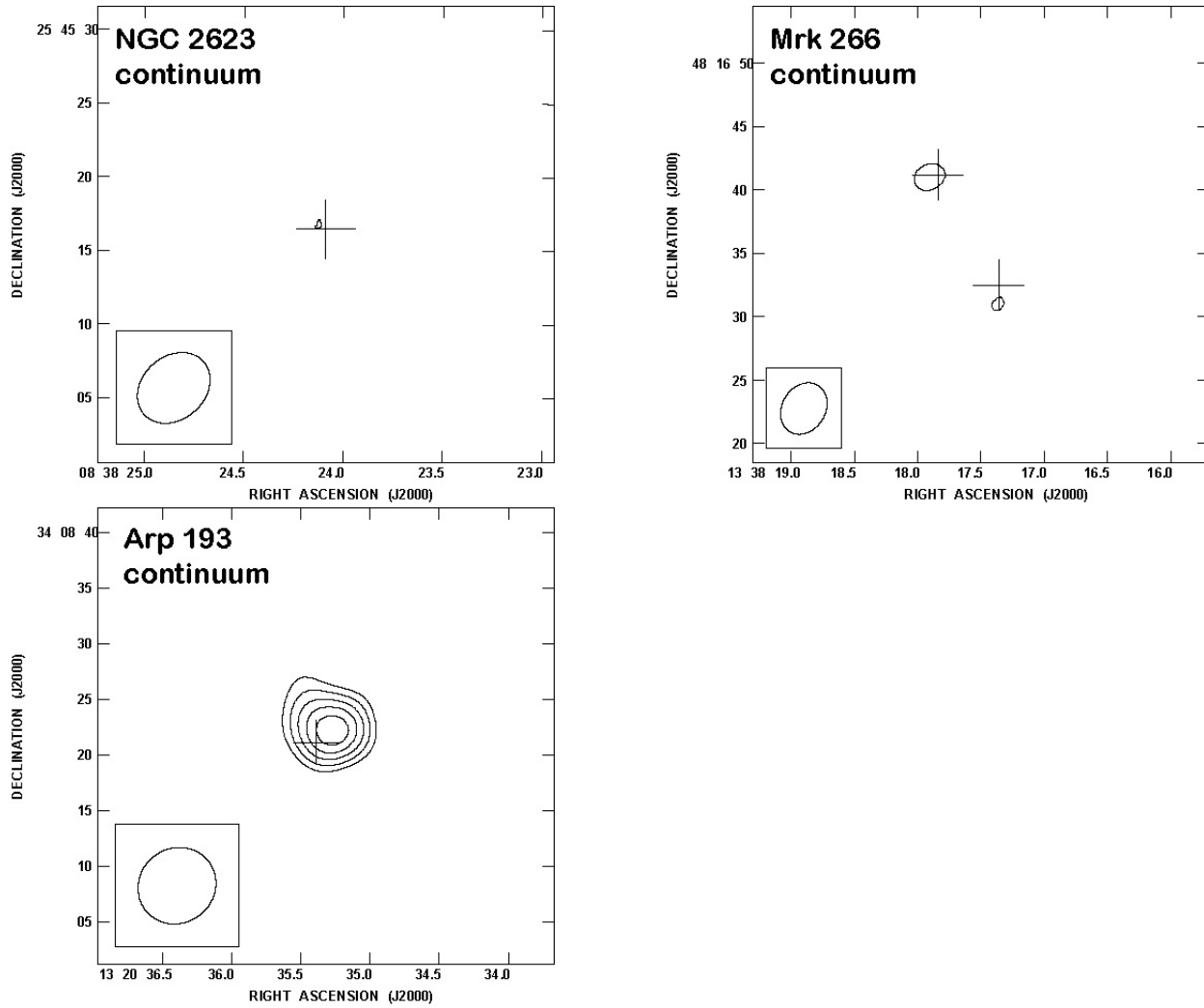
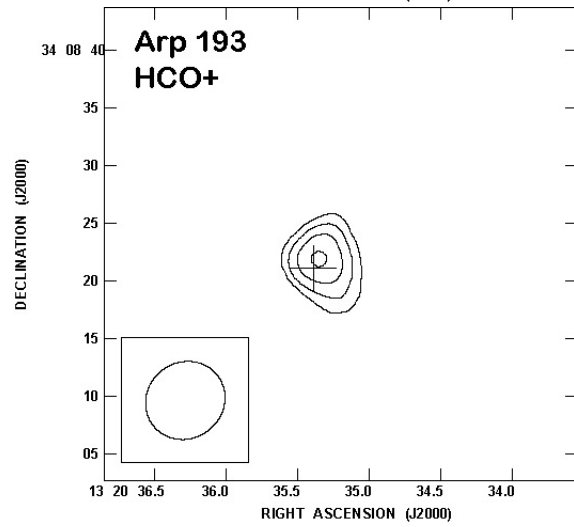
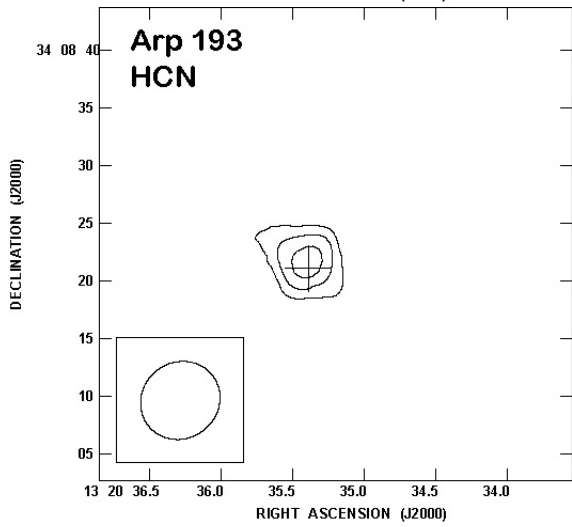
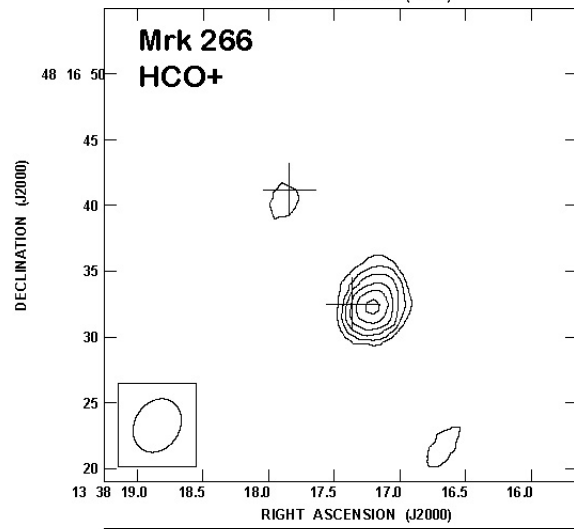
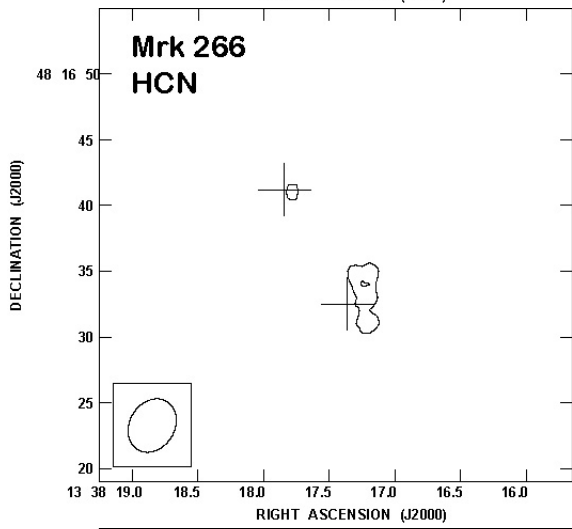
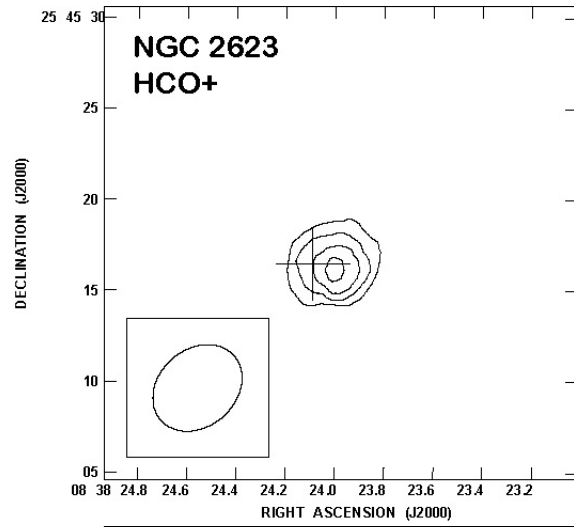
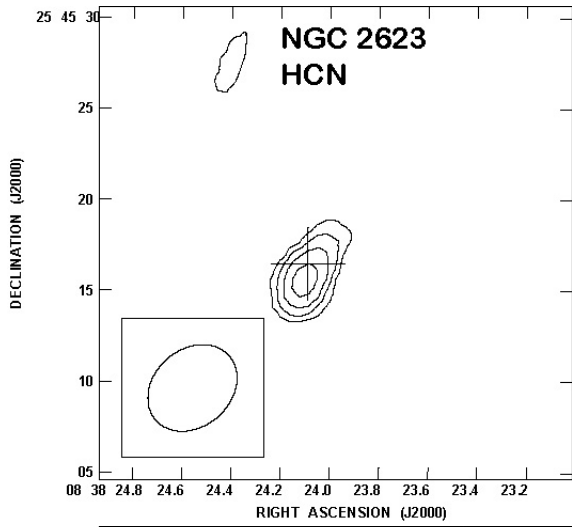


FIG. 1.— Continuum maps of NGC 2623, Mrk 266, and Arp 193 at  $\nu \sim 86\text{--}89$  GHz. The crosses show the coordinates of main nuclei. The coordinates in J2000 are ( $08^{\text{h}}38^{\text{m}}24.09^{\text{s}}$ ,  $+25^{\circ}45'16''.5$ ) for NGC 2623, ( $13^{\text{h}}38^{\text{m}}17.36^{\text{s}}$ ,  $+48^{\circ}16'32''.5$ ) for Mrk 266 SW, ( $13^{\text{h}}38^{\text{m}}17.84^{\text{s}}$ ,  $+48^{\circ}16'41''.1$ ) for Mrk 266 NE, and ( $13^{\text{h}}20^{\text{m}}35.39^{\text{s}}$ ,  $+34^{\circ}08'21''.1$ ) for Arp 193. The nuclear coordinates of NGC 2623 and Arp 193 are adopted from interferometric CO(1–0) maps by Bryant & Scoville (1999), after conversion from B1950 to J2000, using NED. That of Mrk 266 is estimated from *Chandra* X-ray data by Brassington et al. (2007). The contours are  $1.3 \times 3$  mJy beam $^{-1}$  for NGC 2623,  $0.8 \times 3$  mJy beam $^{-1}$  for Mrk 266, and  $1.5 \times (4, 5, 6, 7, 8)$  mJy beam $^{-1}$  for Arp 193. The continuum fluxes at the peak positions are  $\sim 4$  mJy,  $\sim 2.8$  mJy,  $\sim 2.3$  mJy, and  $\sim 15$  mJy for NGC 2623, Mrk 266NE, Mrk 266SW, and Arp 193, respectively. Beam patterns are shown in the small squares at the lower-left corners.



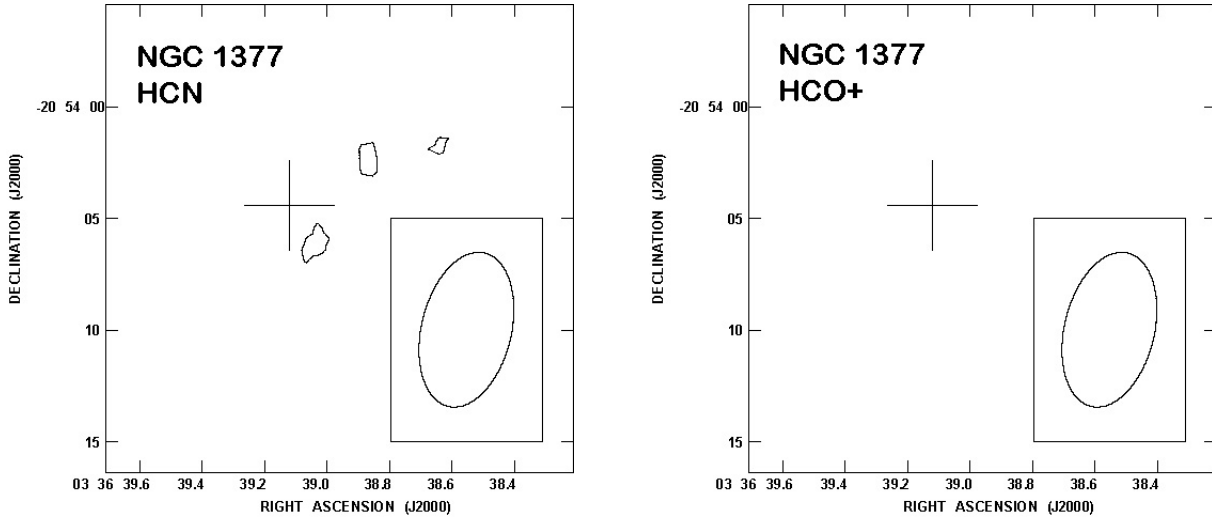


FIG. 2.— *Left*: HCN(1–0) emission map. *Right*: HCO<sup>+</sup>(1–0) emission map. The crosses show the coordinates of main nuclei. For NGC 2623, Mrk 266, and Arp 193, the same coordinates as used in Figure 1 are shown. For NGC 1377, the coordinate in J2000 is (03<sup>h</sup>36<sup>m</sup>39.12<sup>s</sup>, –20°54′04″.4), estimated from optical *B*-band data by Roussel et al. (2006). Continuum emission is subtracted for NGC 2623 and Arp 193, but not for Mrk 266 and NGC 1377 because continuum levels are different for the NE and SW nuclei for Mrk 266 and continuum emission is not detected for NGC 1377 (<2 mJy). For NGC 2623, the contours are  $0.66 \times (4, 5, 6, 7)$  Jy km s<sup>–1</sup> for HCN, and  $0.73 \times (4, 5, 6, 7)$  Jy km s<sup>–1</sup> for HCO<sup>+</sup>. For Mrk 266, the contours are  $0.62 \times (4, 5)$  Jy km s<sup>–1</sup> for HCN, and  $0.55 \times (3, 4, 5, 6, 7, 8)$  Jy km s<sup>–1</sup> for HCO<sup>+</sup>. For Arp 193, the contours are  $1.0 \times (6, 8, 10)$  Jy km s<sup>–1</sup> for HCN, and  $1.0 \times (6, 8, 10, 12)$  Jy km s<sup>–1</sup> for HCO<sup>+</sup>. For NGC 1317, the contours are  $0.5 \times 4$  Jy km s<sup>–1</sup> for HCN, and  $0.5 \times 3$  Jy km s<sup>–1</sup> for HCO<sup>+</sup>.

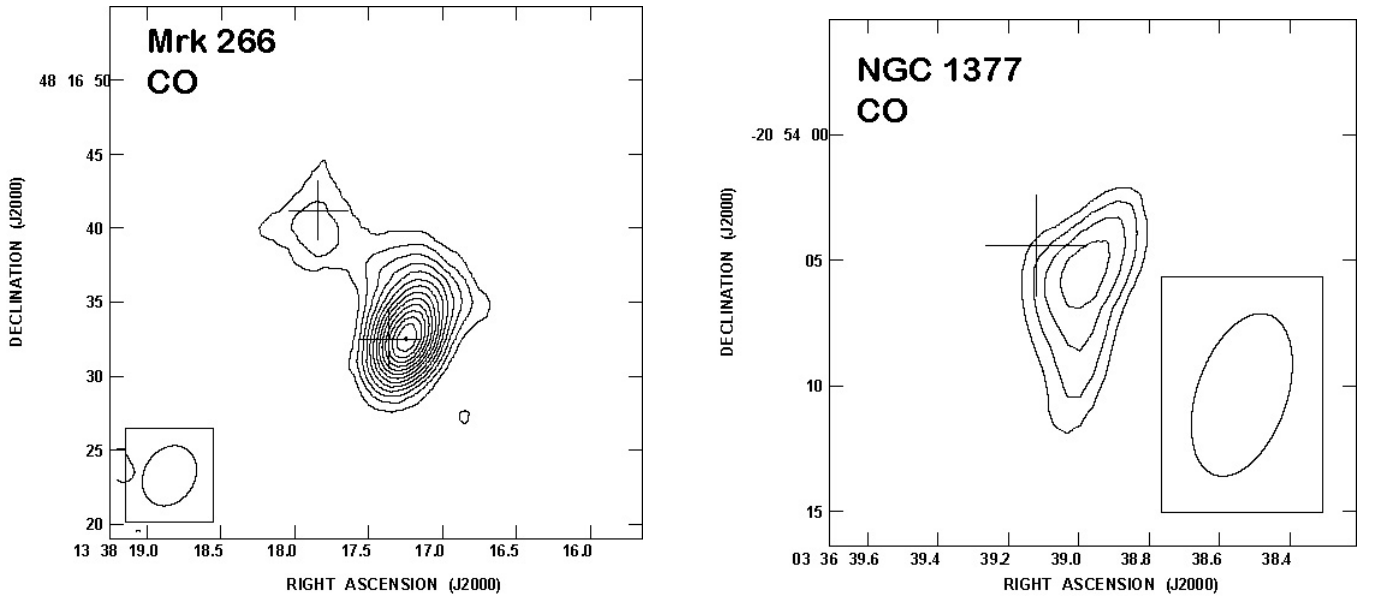


FIG. 3.— CO(1–0) emission for Mrk 266 and NGC 1377. No continuum subtraction was attempted, because the continuum emission is undetected (<5 mJy and <6 mJy for Mrk 266 and NGC 1377, respectively) and negligible compared to the strong CO(1–0) emission. The contours are  $2.85 \times (3, 5, 7, 9, 11, 13, 15, 17, 19, 21, 23, 25, 27, 29)$  Jy km s<sup>–1</sup> for Mrk 266, and  $1.21 \times (5, 6, 7, 8)$  Jy km s<sup>–1</sup> for NGC 1377.

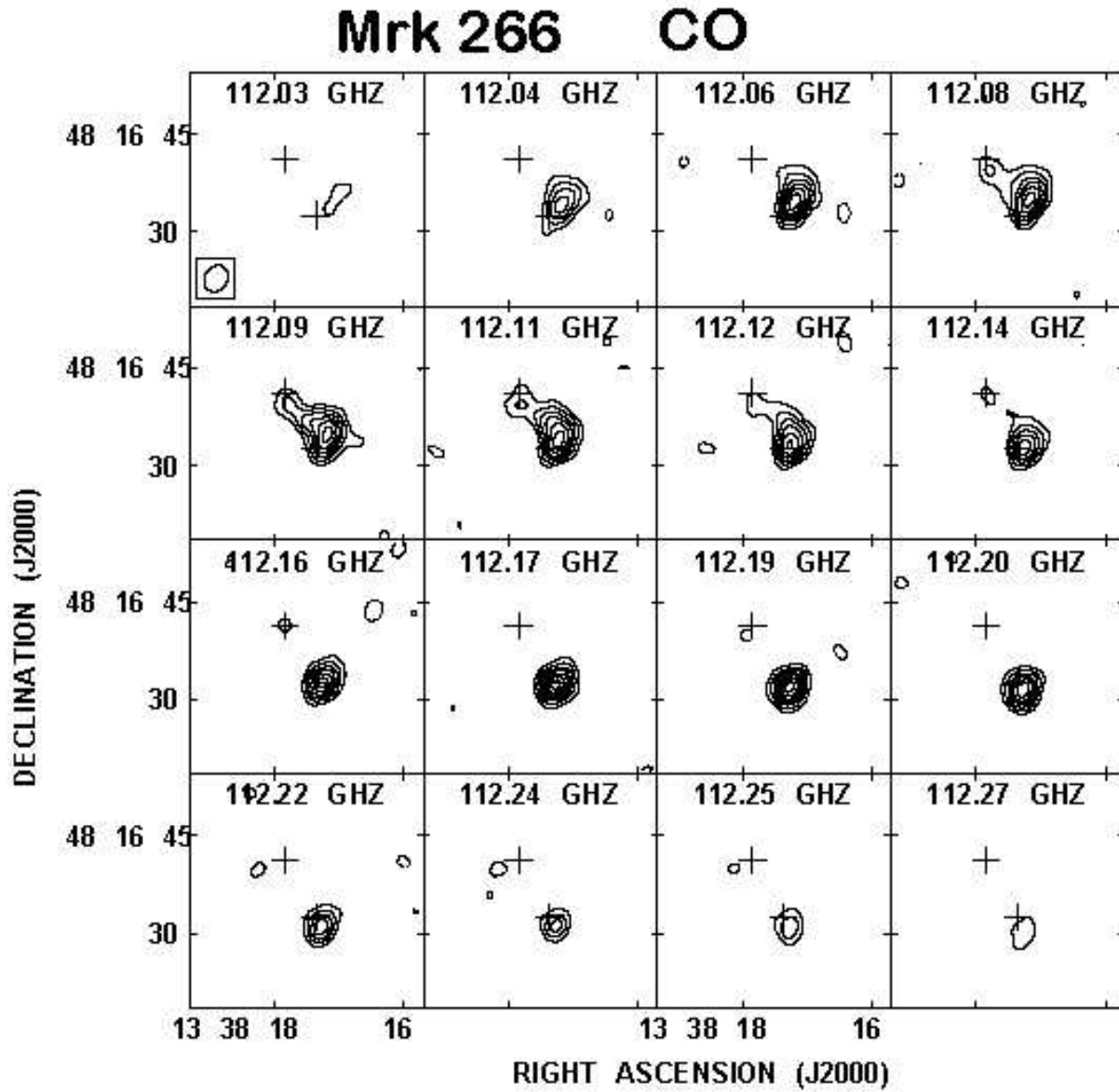


FIG. 4.— Channel map of CO(1-0) emission for Mrk 266. The contours are  $12 \times (-3, 3, 5, 7, 9, 11, 13, 15)$   $\text{mJy beam}^{-1}$ . The rms noise level is  $\sim 12 \text{ mJy beam}^{-1}$ .

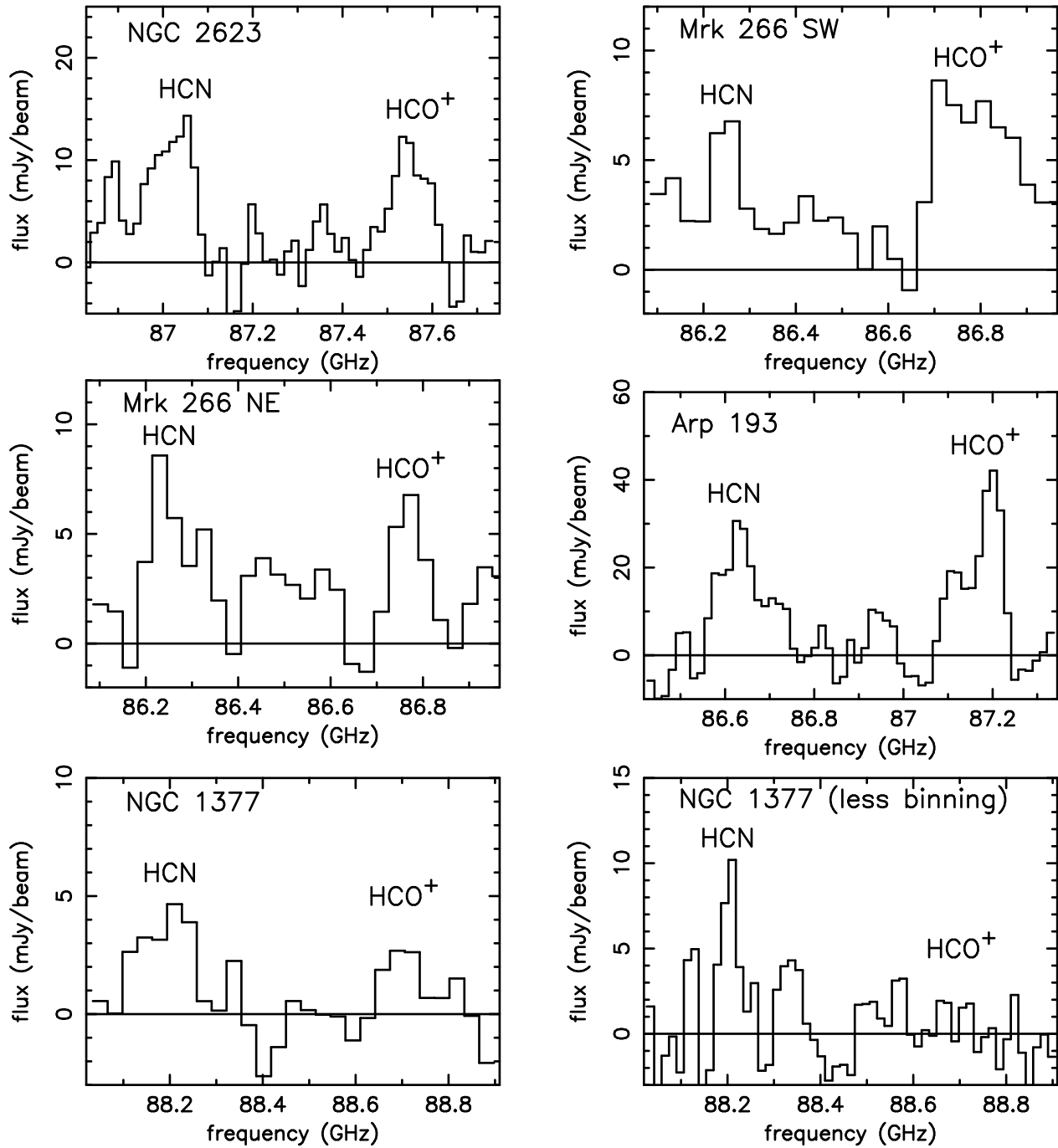


FIG. 5.— HCN(1–0) and HCO<sup>+</sup>(1–0) spectra of observed LIRGs. The abscissa is the observed frequency in GHz and the ordinate is flux in mJy beam<sup>−1</sup>. For NGC 2623 and Arp 193, continuum emission is subtracted, but not for Mrk 266 and NGC 1377. The rms noise levels per spectral bin in the final spectra are  $\sim 4$  mJy (NGC 2623),  $\sim 2.3$  mJy (Mrk 266),  $\sim 7$  mJy (Arp 193),  $\sim 1.8$  mJy (NGC 1377), and  $\sim 2.6$  mJy (NGC 1377, less binning). The horizontal solid line indicates the zero flux level. For the two spectra of NGC 1377, a clean map is first created, and then a spectrum is extracted at the HCN(1–0) peak position in each map.

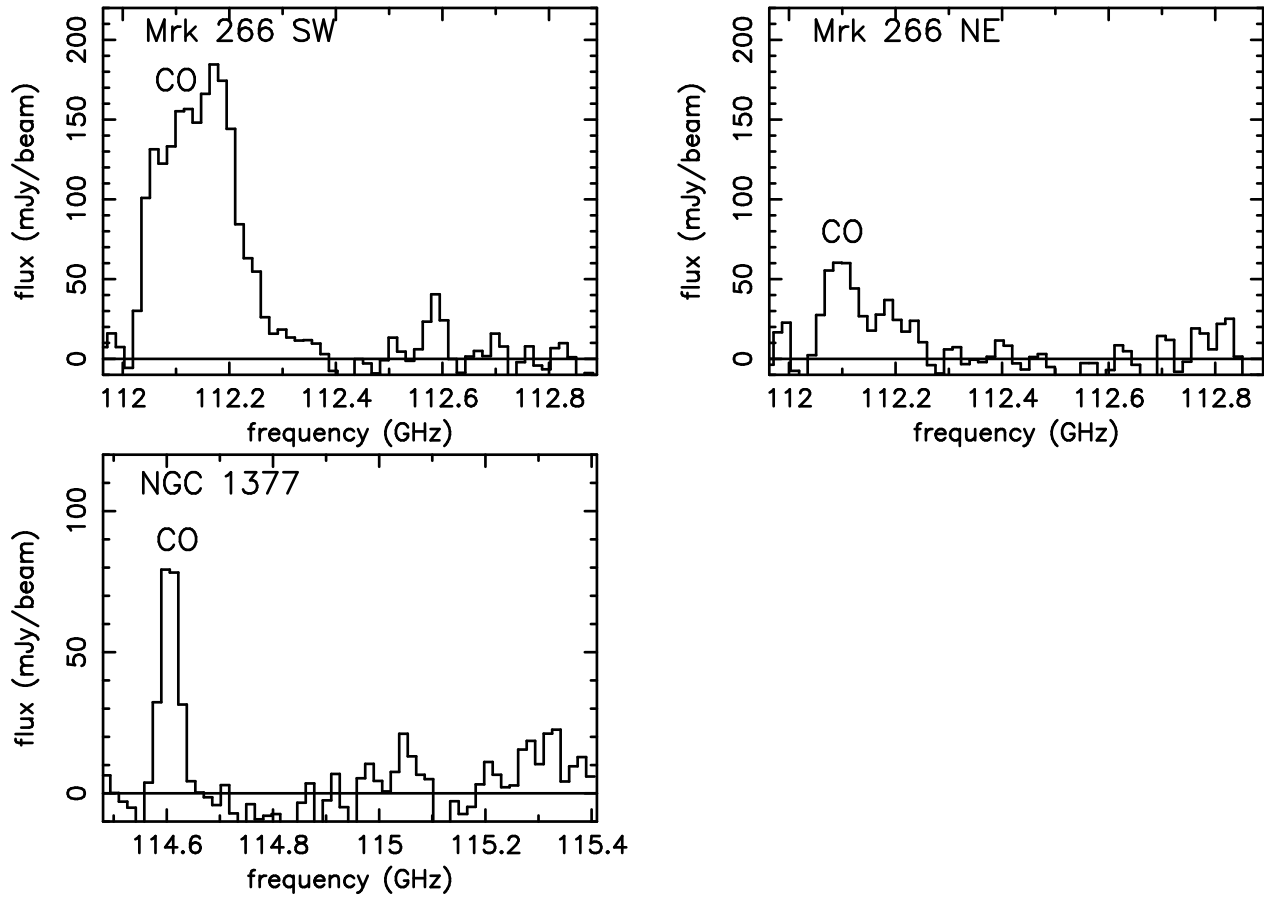
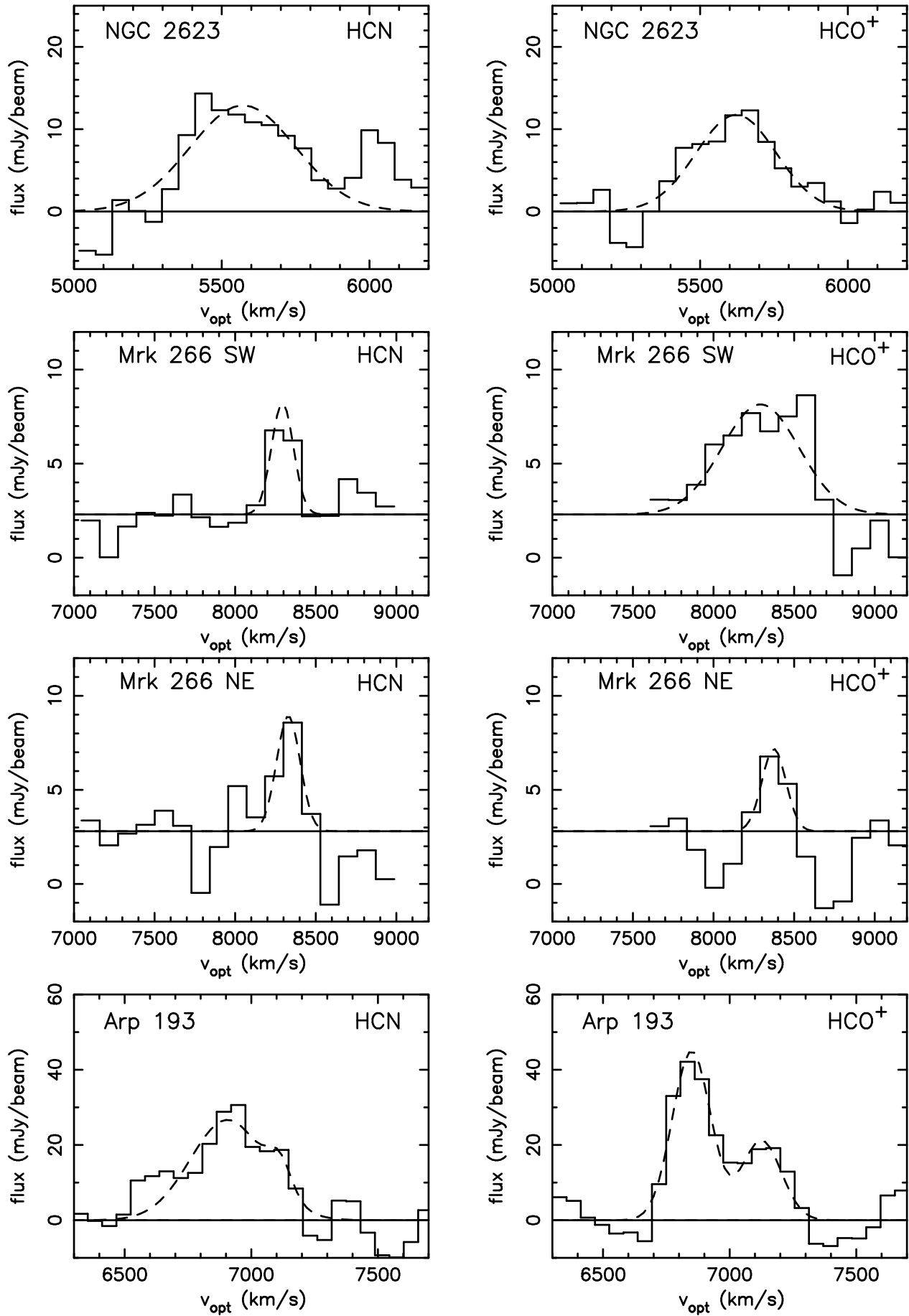


FIG. 6.— CO(1-0) spectra of Mrk 266 and NGC 1377. The abscissa is the observed frequency in GHz and the ordinate is flux in  $\text{mJy beam}^{-1}$ . No continuum subtraction is attempted. The rms noise levels per spectral bin in the final spectra are  $\sim 12$  mJy and  $\sim 9$  mJy for Mrk 266 and NGC 1377, respectively. The horizontal solid line marks the zero flux level.



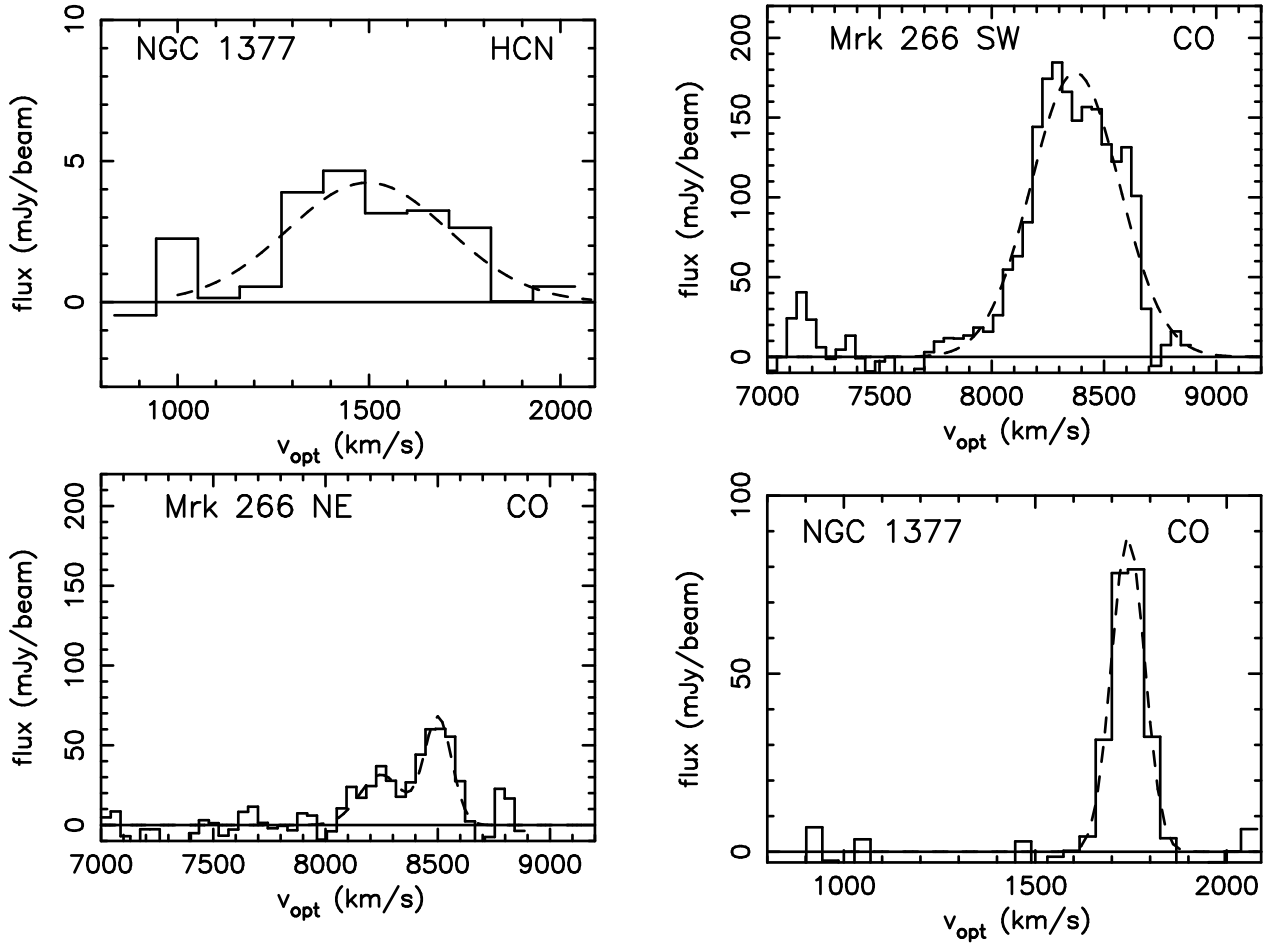


FIG. 7.— Gaussian fits to the detected HCN(1–0), HCO<sup>+</sup>(1–0), and CO(1–0) emission lines. The abscissa is the LSR velocity  $\{v_{\text{opt}} \equiv (\frac{v_{\text{obs}}}{c} - 1) \times c\}$  in km s<sup>−1</sup> and the ordinate is flux in mJy beam<sup>−1</sup>. Although single Gaussian fits are used by default, two Gaussian fits are attempted for double-peaked lines. These lines include HCN(1–0) and HCO<sup>+</sup>(1–0) of Arp 193, and CO(1–0) of Mrk 266 NE. For Arp 193 HCN(1–0), even though the double-peaked signature is not clear, we fit with two Gaussians because the HCN(1–0) profile measured with the IRAM 30-m single-dish telescope (Gracia-Carpio et al. 2008) is double-peaked. For Mrk 266 and NGC 1377, a constant continuum is assumed and is set as a free parameter because continuum emission was not subtracted. For other sources, the continuum level is set as zero. The adopted continuum levels are shown as horizontal solid straight lines for all sources.

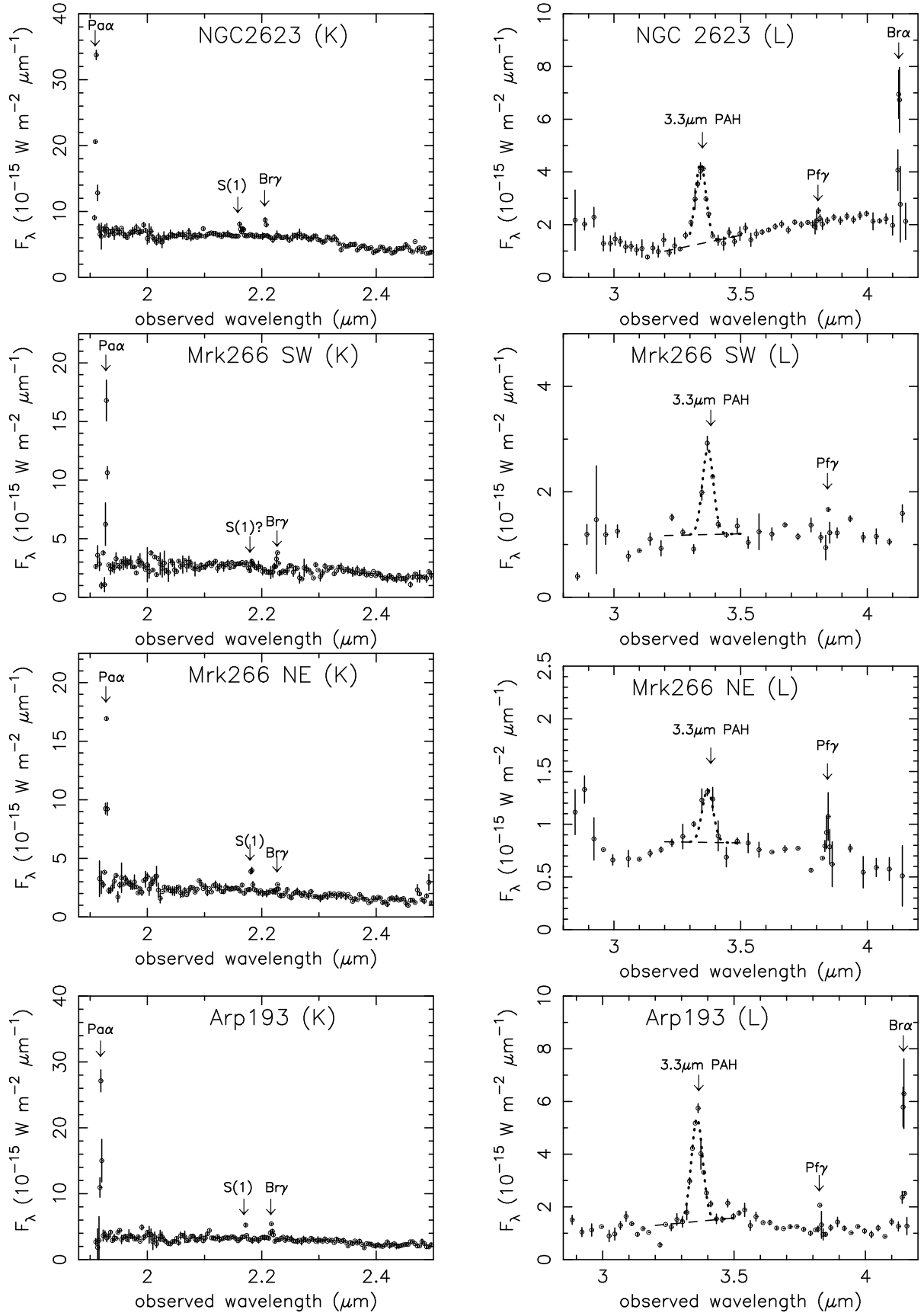


FIG. 8.— Infrared *K*- (1.9–2.5  $\mu\text{m}$ ) and *L*- (2.8–4.2  $\mu\text{m}$ ) band spectra of NGC 2623, Mrk 266, and Arp 193. The abscissa is the observed wavelength in  $\mu\text{m}$ , and the ordinate is flux  $F_\lambda$  in  $10^{-15} \text{ W m}^{-2} \mu\text{m}^{-1}$ . Strong hydrogen recombination lines, Pa $\alpha$  (1.87  $\mu\text{m}$ ), Br $\gamma$  (2.17  $\mu\text{m}$ ), Pf $\gamma$  (3.74  $\mu\text{m}$ ), and Br $\alpha$  (4.05  $\mu\text{m}$ ), the molecular hydrogen H<sub>2</sub>(1–0) S(1) line (2.12  $\mu\text{m}$ ), and the 3.3  $\mu\text{m}$  PAH emission feature are indicated. The mark “?” indicates that detection is unclear. The dashed lines are the adopted continuum levels for the 3.3- $\mu\text{m}$  PAH emission feature, and the dotted lines indicate the fittings of the 3.3- $\mu\text{m}$  PAH emission using the template profile (§4.2.3).

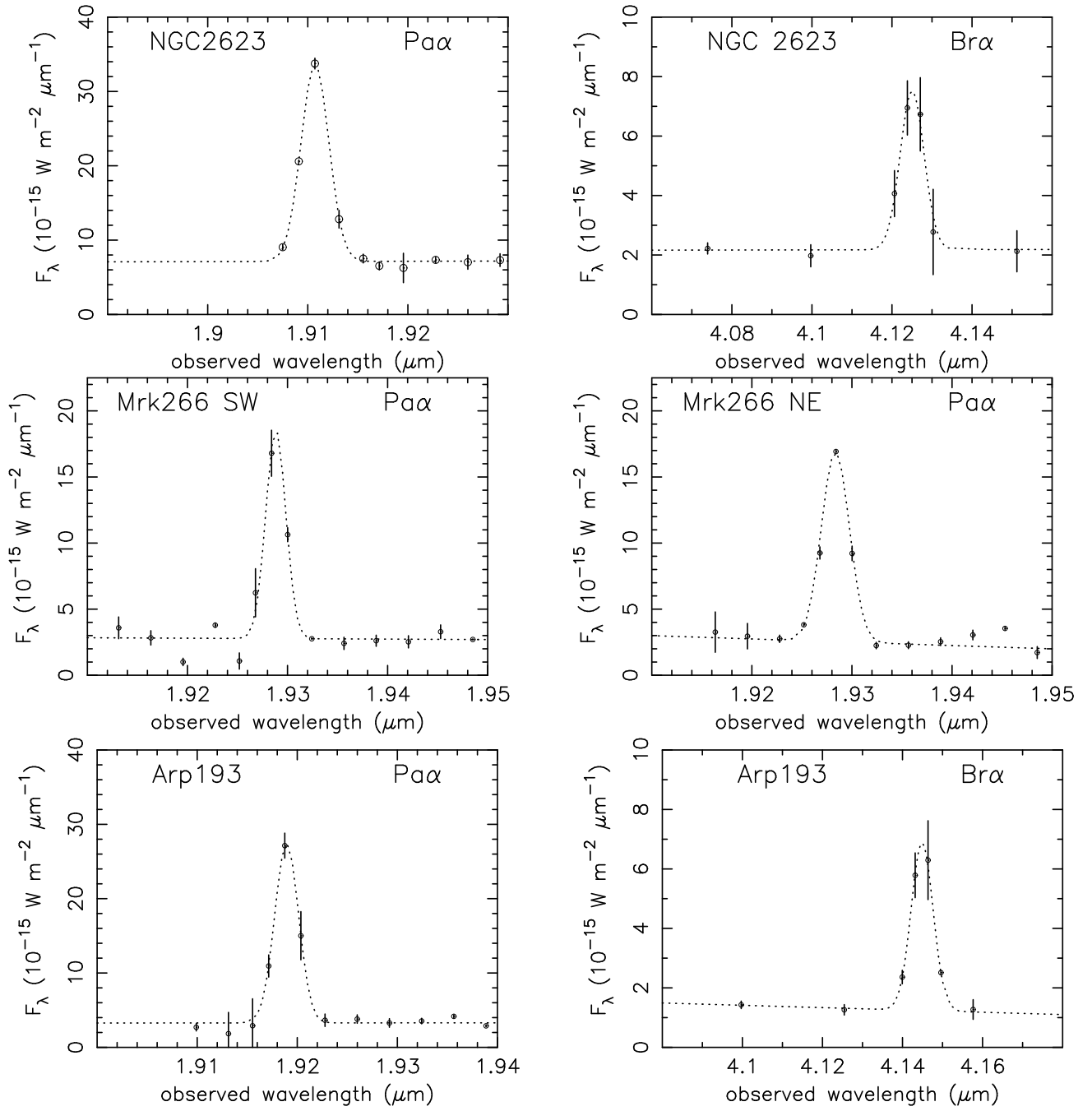


FIG. 9.— Enlarged spectra around Pα and Brα emission lines. The abscissa is the observed wavelength in  $\mu\text{m}$ , and the ordinate is flux  $F_\lambda$  in  $10^{-15} \text{ W m}^{-2} \mu\text{m}^{-1}$ . Gaussian fits are overlotted as dotted lines.

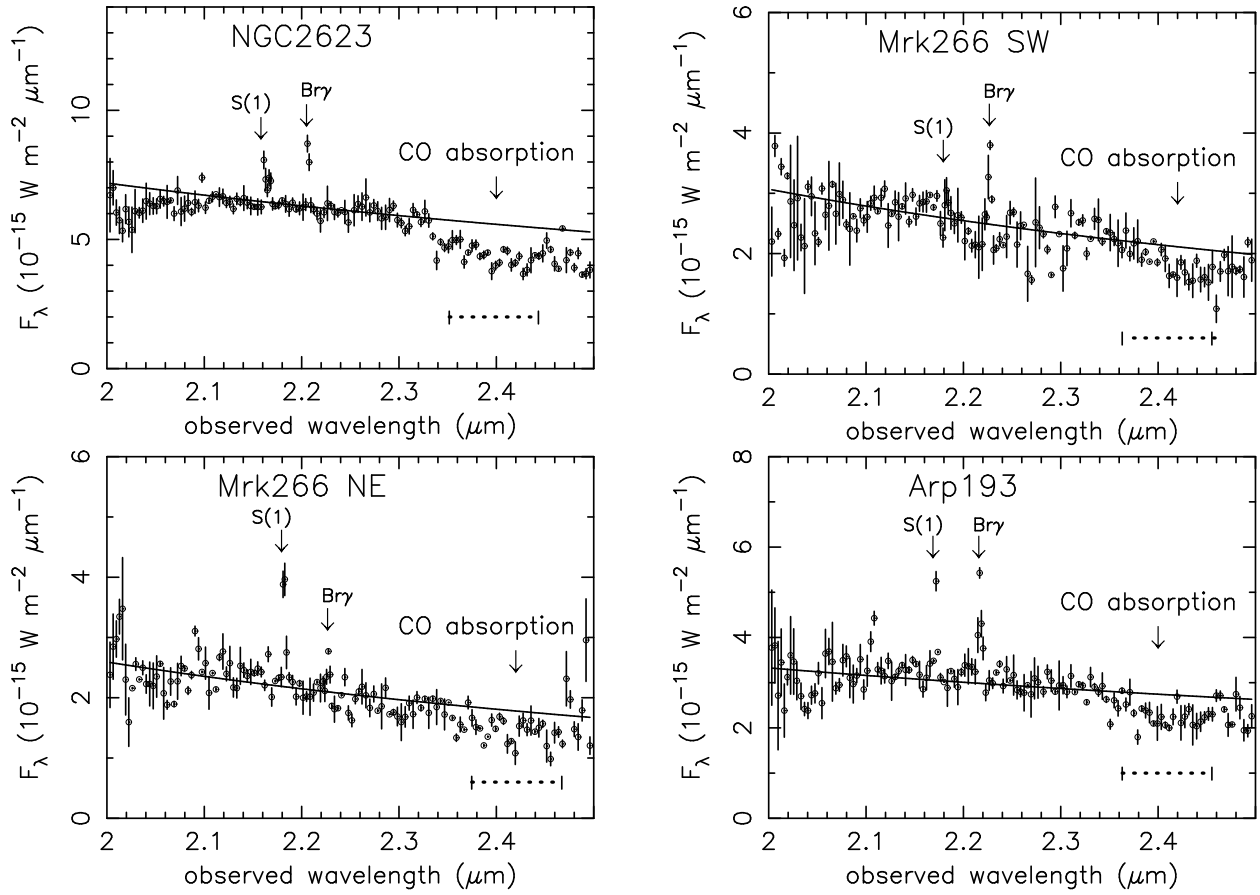


FIG. 10.— Enlarged spectra around the 2.3–2.4  $\mu\text{m}$  CO absorption features. The abscissa is the observed wavelength in  $\mu\text{m}$ , and the ordinate is flux  $F_\lambda$  in  $10^{-15} \text{ W m}^{-2} \mu\text{m}^{-1}$ . The dotted lines inserted with vertical solid lines mark the wavelength range used to measure the  $\text{CO}_{\text{spec}}$  values, against the adopted continuum levels shown as solid lines.

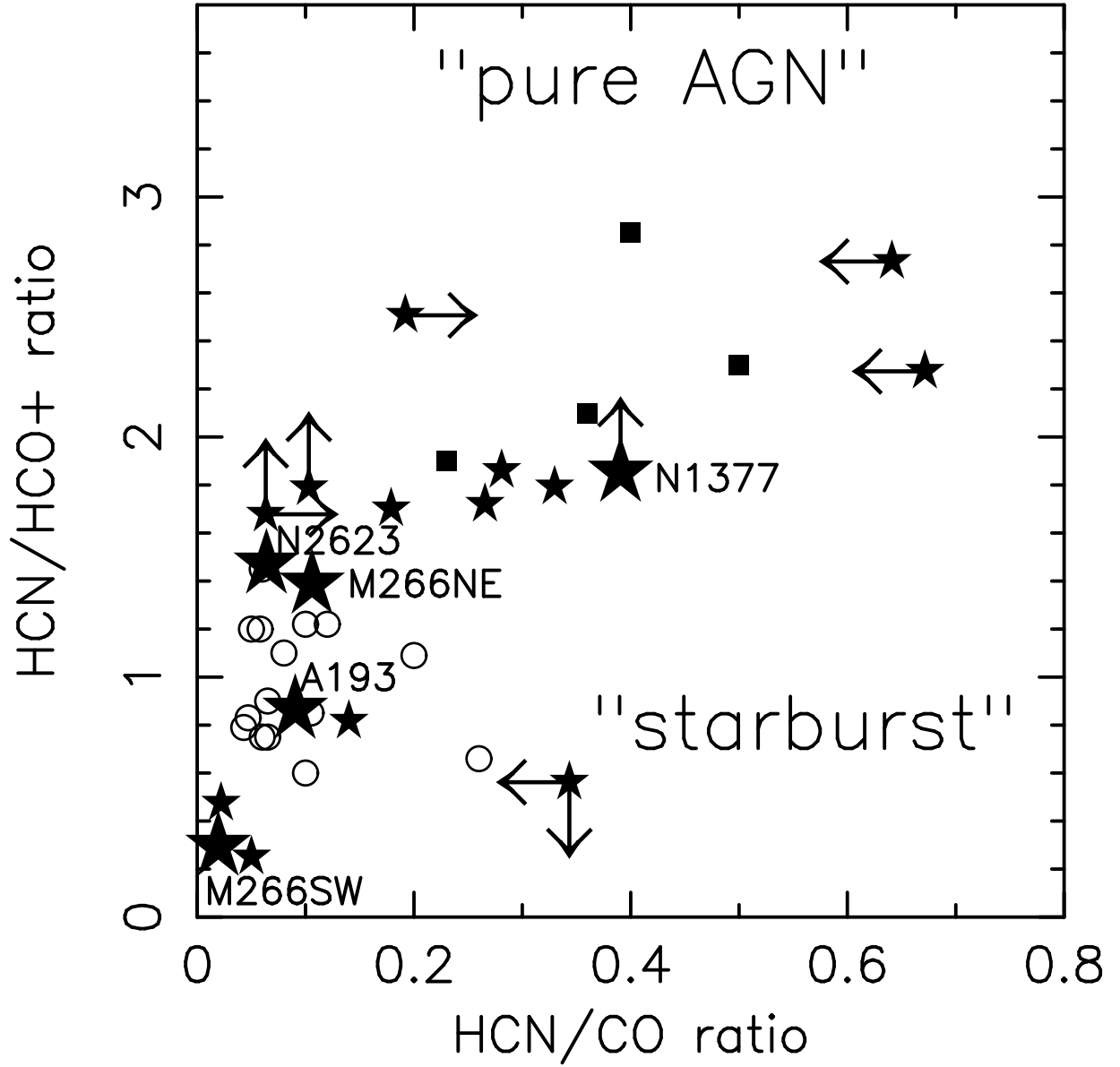


FIG. 11.— HCN(1–0)/HCO<sup>+</sup>(1–0) (ordinate) and HCN(1–0)/CO(1–0) (abscissa) ratios in brightness temperature ( $\propto \lambda^2 \times$  flux density), derived from our NMA interferometric observations. NGC 2623, Mrk 266 SW and NE, Arp 193, and NGC 1377 are plotted as large filled stars with labels. Other LIRGs previously observed by Imanishi et al. (2004, 2006b, 2007b) and Imanishi & Nakanishi (2006) are also plotted as small filled stars. Other data points are taken from Kohno (2005), where sources with AGN-like (starburst-like) ratios are marked with filled squares (open circles). For all LIRG nuclei, the HCN(1–0)/HCO<sup>+</sup>(1–0) brightness-temperature ratios in the ordinate are those toward the nuclei, where putative buried AGNs are expected to reside. Contamination from extended star-forming emission outside the beam sizes (Table 3) is totally removed.

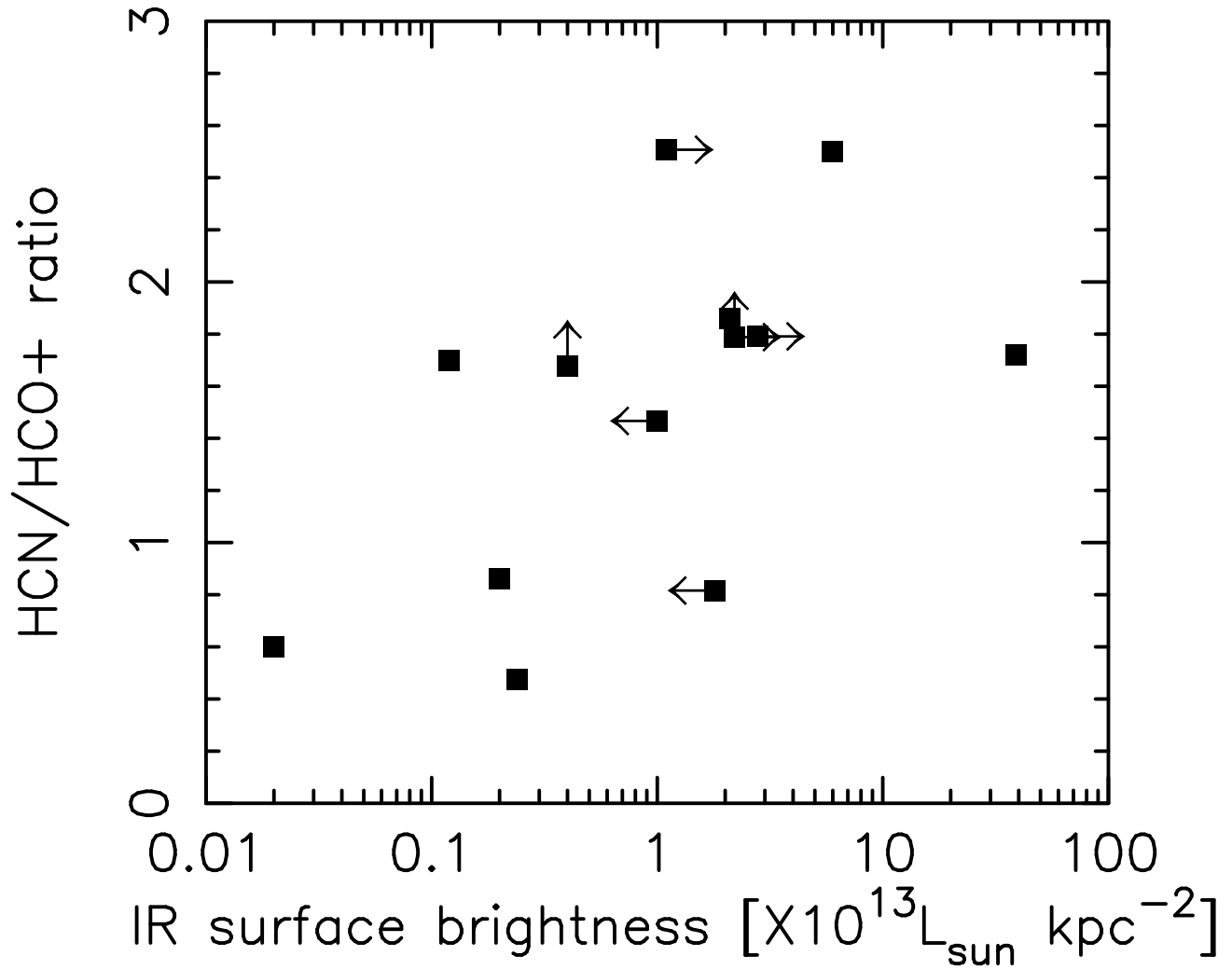


FIG. 12.— HCN(1–0)/HCO<sup>+</sup>(1–0) brightness-temperature ratio (ordinate) and infrared emission surface brightness (abscissa) for LIRGs with available infrared emission surface brightness data (Soifer et al. 2000, 2001; Evans et al. 2003). Only LIRGs whose HCN(1–0) and HCO<sup>+</sup>(1–0) lines were simultaneously observed with NMA, and the prototypical starburst galaxy M82 (Kohno et al. 2001), are plotted. The LIRG sample includes IRAS 08572+3915, UGC 5101, Mrk 231, Mrk 273, Arp 220, IRAS 17208–0014, VV 114 E, Arp 193, NGC 2623, Arp 299 A and C, and NGC 4418 (Imanishi et al. 2004, 2006b; Imanishi & Nakanishi 2006; Imanishi et al. 2007b). For Arp 220, the HCN(1–0)/HCO<sup>+</sup>(1–0) brightness-temperature ratio is the average value of the eastern and western nuclei (Imanishi et al. 2007b).